Transport in Porous Media (2024) 151:2647–2692
https://doi.org/10.1007/s11242-024-02125-5

Investigation of Different Throat Concepts for Precipitation Processes in Saturated Pore-Network Models

Theresa Schollenberger[1] · Lars von Wolff[2] · Carina Bringedal[3] · Iuliu Sorin Pop[4] · Christian Rohde[2] · Rainer Helmig[1]

Received: 21 May 2024 / Accepted: 31 August 2024 / Published online: 8 October 2024

Abstract

The development of reliable mathematical models and numerical discretization methods is important for the understanding of salt precipitation in porous media, which is relevant for environmental problems like soil salinization. Models on the pore scale are necessary to represent local heterogeneities in precipitation and to include the influence of solution-air-solid interfaces. A pore-network model for saturated flow, which includes the precipitation reaction of salt, is presented. It is implemented in the open-source simulator DuMu$^{\mathrm{X}}$. In this paper, we restrict ourselves to one-phase flow as a first step. Since the throat transmissibilities determine the flow behaviour in the pore network, different concepts for the decreasing throat transmissibility due to precipitation are investigated. We consider four concepts for the amount of precipitation in the throats. Three concepts use information from the adjacent pore bodies, and one employs a pore-throat model obtained by averaging the resolved pore-scale model in a thin-tube. They lead to different permeability developments, which are caused by the different distribution of the precipitate between the pore bodies and throats. We additionally apply two different concepts for the calculation of the transmissibility. One obtains the precipitate distribution from analytical assumptions, the other from a geometric minimization principle using a phase-field evolution equation. The two concepts do not show substantial differences for the permeability development as long as simple pore-throat geometries are used. Finally, advantages and disadvantages of the concepts are discussed in the context of the considered physical problem and a reasonable effort for the implementation and computational costs.

✉ Theresa Schollenberger
theresa.schollenberger@iws.uni-stuttgart.de

[1] Institute for Modelling Hydraulic and Environmental Systems, University of Stuttgart, Pfaffenwaldring 61, 70569 Stuttgart, Germany

[2] Institute of Applied Analysis and Numerical Simulation, University of Stuttgart, Pfaffenwaldring 57, 70569 Stuttgart, Germany

[3] Department of Computer Science, Electrical Engineering and Mathematical Sciences, Western Norway University of Applied Science, Inndalsveien 28, 5063 Bergen, Norway

[4] Faculty of Sciences, Hasselt University, Agoralaan Gebouw D, 3590 Diepenbeek, Belgium

Article Highlights

- **Presentation of a pore-network model for single-phase flow with salt precipitation including pore-space alterations**
- **Different concepts to calculate the amount of precipitation in throats and the throat transmissibility are presented**
- **Between the concepts large differences in the permeability and precipitation distribution are observed in the network**

Keywords Pore-network model · Salt precipitation · Porous-media flow · Numerical simulations

Variables

A_{ij}	Cross-sectional area of pore throat ij, m^2
A_ϕ	Debye–Hückel constant, –
A_{react}	Reactive surface area of pore body, m^2
$A_{\text{pn},x}$	Cross-sectional area of the pore-network system perpendicular to x coordinate, m^2
a_i	Pore-throat radius adjacent to pore body i, m
B	Height width ratio for rectangular throat cross section, –
b	Characteristic constant for Pitzer approach, $\sqrt{\text{kg mol}^{-1}}$
C	Salt specific constant for Pitzer approach, –
D_{m}	Molecular diffusion coefficient, $m^2\ s^{-1}$
$d(\phi)$	Function for Navier-slip length
d	Circular throat cross-section diameter, m
f_{throat}	Volume fraction from the total precipitated volume, that is located in the throats, –
h	Height of rectangular cross-section shape, m
h_{ref}	Reference side length of the computational domain of the phase-field model, m
I	Ionic strength, –
IAP	Ionic activity product, –
$[ion]$	Activity of a specific ion, –
$K_{\text{pn},x}$	Permeability of the pore-network system for flow in x-direction, m^2
K_{eq}	Equilibrium constant, –
k	Reaction constant, $\text{mol m}^{-2}\ \text{s}^{-1}$
l_{ij}	Length of pore throat ij: $l_{ij} = z_j - z_i$, m
M^κ	Molar mass of component κ, kg mol^{-1}
M	Mobility (non-dimensionalized), –
m	Molality, mol kg^{-1}
N_{in}	Number of pore throats with incoming flux, –
N	Number of connected pore throats to a pore body, –
$N_{\text{pn,body}}$	Total number of pore bodies in pore network, –
$N_{\text{pn,throat}}$	Total number of pore throats in pore network, –
n	Throat section, –
p	Pressure, $\text{kg m}^{-1}\ \text{s}^{-2}$
Q	Volume flux, $m^3\ s^{-1}$
Q_{m}	Molar flux, mol s^{-1}
$Q_{\text{mass,pn},x}$	Total mass flux leaving pore-network system through area perpendicular to x-direction, kg s^{-1}

$q(\phi)$	Function to locate precipitation reaction, –
$\mathcal{R}$	Precipitation rate (non-dimensionalized), –
R	Pore-body radius, m
r	Radius of circular throat cross-section shape, m
s_i	Source term of pore body i including chemical reaction, mol s^{-1}
T	Temperature, K
t	Time, s
Δt	Time step size, s
g_{ij}	Pore-throat transmissibility, m^4 s kg^{-1}
u	Protonic units, –
V	Volume of pore body or throat, m^3
V_s	Volume of solid salt in a pore body or throat, m^3
v_z	Longitudinal velocity of pore throat (non-dimensionalized), –
v	Darcy velocity, m s^{-1}
W	Double well function, –
w	Width of rectangular cross-section shape, m
X	Cation
x	Mole fraction, –
$x_{\max}^{\mathrm{NaCl}}$	Mole fraction of solubility limit of NaCl, –
Y	Anion
y	Number of ions, –
z	Z-coordinate along the pore throat
β	Salt specific constant for Pitzer approach, –
δ	Thickness of the precipitated salt layer, m
γ	Activity coefficient, –
ρ_m	Molar density, mol m^{-3}
ρ	Mass density, kg m^{-3}
ϕ	Phase-field variable, –
ϕ_s	Volume fraction of the solid phase volume over the initial pore volume, –
ϵ	Phase-field parameter, –
μ_c	Chemical potential (non-dimensionalized), –
μ	Viscosity, kg m^{-1} s^{-1}
Ω	Saturation index, –

Subscripts

avg	Arithmetical average over whole pore network
body	Pore body
circ	Circular throat cross section
ini	Initial condition
i	Pore body i
ij	Pore throat connecting pore body i and j
j	Pore body j adjacent to pore body i
n	Pore-throat section
rect	Rectangular throat cross section
s	Solid phase
v	Number of ions
pn	Parameter describing whole pore-network system

Superscripts

Cl^-	Chloride anion
ion	Ion of the salt component
NaCl	Salt component
Na^+	Sodium cation
t	Time step
Δt	Change between two time steps
w	Water component
z	Protonic units of the cation and anion
κ	Component
^	Non-dimensional
¯	Variable averaged over the throat cross section and consequently depending only on z (used in CAP4)
~	Variable depending on all three dimensions x, y and z (used in CAP4)

Abbreviations

CAP	Concept for the amount of precipitation
CAP1	Concept of relative pore-body volume change from Nogues et al. (2013)
CAP2	Concept of average precipitation source
CAP3	Concept of linear growth
CAP4	Concept of a thin tube
CT	Concept for pore-throat transmissibility
CT1	Concept of Bruus (2011)
CT2	Phase-field model concept
REV	Representative elementary volume

1 Introduction

Salt precipitation is an important process in many environmental and technical applications like e.g. soil salinization (Shahid et al. 2018; Wicke et al. 2011) or precipitation in building material (Scherer 2004; Espinosa et al. 2008). Soil salinization for example describes salt precipitation in the subsurface and is a severe problem in arid and semi-arid regions, like Australia (Ondrasek et al. 2011; Rengasamy 2006), the Mediterranean coastline (Daliakopoulos et al. 2016) or India (Sharma and Singh 2015). Due to high evaporation rates, dissolved salt is transported towards the soil surface, where the water evaporates and salt accumulates. When the solubility limit of the salt is exceeded, salt precipitates and forms solid salt, which transforms the pore space. The high salt concentrations and precipitated salt lead to degradation of land, a reduction of plant growth and crop yield, resulting in economic losses (Munns and Tester 2008; Singh 2015; Qadir et al. 2014; Wicke et al. 2011).

Mathematical modelling and numerical simulations are essential for gaining a thorough understanding of the relevant processes as they provide essential information without employing complex, or even unfeasible experiments. Numerical simulations enable to identify the influence of different parameters like porous-media properties, evaporation rate or salt properties on the precipitation process and the development of the pore space. The necessary model, capturing the relevant physical processes of soil salinization, has to consider two fluid phases, air and saline solution, and the solid phase of precipitated salt. The process of evaporation has to be included, as well as the chemical reaction of precipitation.

The chemical reaction describes the precipitation of the dissolved salt in the water phase as solid salt phase. Further, the alteration of the pore space due to the precipitation has to be considered.

Such mathematical models can be developed at different scales. One can consider the processes at either the scale of pores, or at the scale of a representative elementary volume (REV-scale). In REV-scale models (e.g. Agosti et al. 2015; Jambhekar et al. 2016; Kala and Voskov 2020), no distinction is made between the pore space and the solid mineral. The porous-medium properties are averaged over a REV, as well as the precipitated solid salt, the fluid velocity and pressure, and the solute concentration. The models are capable to describe the averaged behaviour of the system. A major drawback is in the assumptions made on the relationships between different model quantities, e.g. how the evolution of the porosity or the permeability depends on the amount of precipitated mineral. Such models are efficient from a computational point of view, but less accurate since the pore-scale details are lost.

However, pore-scale processes could have a large influence on the precipitation processes. In particular, the interfaces between salt-solution, air and solids are process controlling (Norouzi Rad et al. 2013; Rad et al. 2015), about which no information is available on the REV-scale. Further, local heterogeneities in precipitation cannot be represented in REV-scale models as the distribution of the precipitated salt is averaged over the REV. To incorporate this information models on the pore-scale are necessary.

On the pore scale different kinds of models are available (Steefel et al. 2013; Golparvar et al. 2018). On the one hand, there is direct pore-scale modelling which resolves the pore space in detail, like lattice Boltzmann models (Kang et al. 2003; Yoon et al. 2015; Liu et al. 2016; Yang et al. 2023), a pseudo-molecular method, or computational fluid dynamics (Molins et al. 2012; Molins 2015; Zaretskiy et al. 2010), which solves the Navier–Stokes equation with numerical, grid-based methods. All processes are described in detail, in particular the alteration of the pore space, but the models become extremely complex and the simulations are expensive, if not unfeasible. On the other hand, there are pore-network models (Blunt 2017; Raoof et al. 2010; Nogues et al. 2013; Weishaupt et al. 2019) which represent the pore space with distinct pore-scale elements. Pore-network models are computationally more efficient through the simplified representation of the pore space and consequently suitable to model larger samples. The pore space is modelled with a network of pore bodies, representing larger pore spaces, and pore throats, representing the narrow connections in between, see Fig. 1. Here though, the explicit form of the precipitate is not resolved in detail as it is averaged over the pore bodies and throats. It appears as

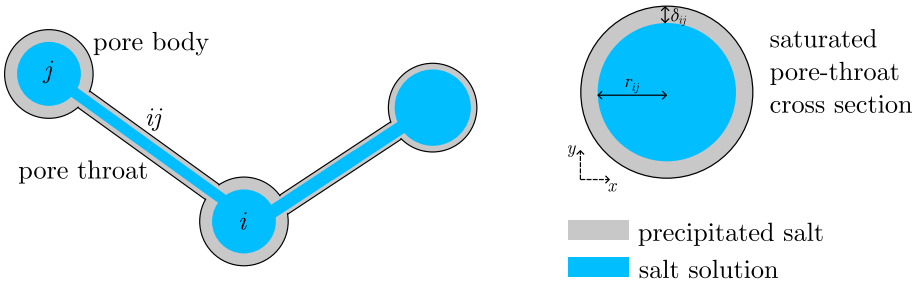

Fig. 1 Scheme of the pore-network model: the general structure of the pore network on the left and the scheme for a circular cross section of a saturated pore throat on the right

a solid volume fraction in the individual elements and mainly just influences the volume and cross-sectional area of the elements. A detailed introduction to pore-network models is given by Blunt (2017).

An efficient tool to bridge the gap between models at the pore scale and those at the REV scale is upscaling, for which direct pore-scale modelling (Gahn and Pop 2023; Schulz et al. 2017; Bringedal et al. 2020; Luo et al. 2012) as well as pore-network models (Li et al. 2006) can be used. Furthermore, pore-network models can be coupled with REV-scale models (Weishaupt 2020) to allow the simulation of larger areas and still consider the pore-scale processes in relevant areas with high process activity.

In addition, there are different possibilities to describe the alteration of the pore space on the pore-scale. We restrict the discussion here to dissolution and precipitation processes in a porous medium. One can track specifically the interface separating the mineral and the fluid (the pore walls), by either considering this as a free boundary (van Noorden 2009; Kumar et al. 2011; Bringedal et al. 2016; Eden et al. 2022), or as the 0-level set of a function that, on its turn becomes an unknown of the model (van Noorden 2008; Bringedal and Kumar 2017). However, in both approaches the pore space is time dependent and has an a priori unknown evolution, which complicates the numerical simulations significantly. To avoid this, one may use phase fields to approximate the free boundary by a thin, diffuse interface domain (van Noorden and Eck 2011; von Wolff and Pop 2022). In this way, the resolved pore-scale model can be stated in a fixed domain. In this context, we mention Kelm et al. (2022), where different modelling approaches are compared.

In this work, a pore-network model was chosen to simulate the precipitation process as it is a good compromise that represents the processes on the pore scale in detail and is still relatively computationally efficient. In the pore-network model a mass balance is solved for each pore body, which stores one set of primary variables as average values of the respective pore body (Blunt et al. 2002; Dashtian et al. 2018). The volume of the throat is either neglected or transferred to the pore bodies. Fluxes are calculated in the pore throats based on the pressure and concentration differences between the adjacent pore bodies and the geometry-based flow resistance of the throat. There are also pore-network models available which solve mass balance equations for pore bodies as well as for pore throats. In Raoof et al. (2010) for example, such a pore-network model is presented for simulating transport and adsorption.

In case of not solving a mass balance in the pore throats, certain challenges concerning salt precipitation arise. Here, the determination of the precipitated volume and the resulting transmissibility in the pore-throat is not straightforward. In pore-network models the amount of precipitate in the pore bodies can be calculated based on the salt concentration in the respective pore body and the solubility limit of the salt. This is used to calculate the decrease of the pore-body volume. In case of only solving the mass balance in the pore bodies, no information about the salt concentration in the pore throats is available. Thus, assumptions have to be made for the calculation of the amount of precipitate in the throat and the resulting narrowing of the throat. The narrowing of the throats increases the flow resistance and hence decreases the transmissibility of the throats, which has a great influence on the overall flow behaviour in the pore network. In addition, assumptions are needed on the shape in which the salt precipitates on the pore-throat walls. This also influences the transmissibility of the pore throat.

In this paper we introduce a pore-network model for salt precipitation for one fluid phase. In particular, different concepts are introduced and compared, which represent the geometry alterations of saturated pore throats due to precipitation in pore-network models. The analysis in this paper discusses the characteristics and differences of the concepts but

is not able to determine the most physical concept. To answer this question, future comparisons with experiments are necessary.

In this paper, sodium chloride NaCl is used as only salt species for simplicity. A precipitation model for several salt species can e.g. found in Mejri et al. (2017, 2020) for the REV-scale. Further, only saturated pore throats are considered as a first step. The development of the concepts, however, is made with regard to further extension to the final model considering two fluid phases. The concepts developed for the single-phase model can later also be applied in a two-phase model, in particular for saturated throats but also in case of invaded throats assuming film flow.

The pore-network model presented in Weishaupt et al. (2019) and implemented in the open-source simulator DuMu$^{\text{X}}$ (Koch et al. 2018, 2020) is extended in this paper to model salt precipitation and the resulting pore-space alterations. In this model, the volume of the pore throats is transferred to the pore bodies and the mass balance is only solved for each pore body. No separate mass balance for the throats is considered.

To model the precipitation in the throats, in a first step the amount of precipitated salt in the throat and the resulting throat volume is determined. In a second step the new dimensions of the throat and the transmissibility are calculated based on the amount of precipitation determined in the first step. For the first step, four different concepts for the amount of precipitation (CAPs) are developed and for the second step, two concepts for the calculation of the pore-throat transmissibility (CTs) are introduced. Both types of concepts CAP and CT can be used in different combinations.

The four different CAPs are first a concept using the relative pore-body volume change and is introduced by Nogues et al. (2013) (CAP1), second a concept using an average source term (CAP2), third a concept of linear growth (CAP3), and fourth a concept of a thin tube (CAP4). Further two different CTs are introduced, which are based on different assumptions about the shape of the precipitate. The first concept (CT1) calculates the transmissibility using analytical relations derived by Bruus (2011). For the second concept (CT2), a phase-field model is used. The underlying assumptions of the different concepts are discussed in detail and their influence on the pore-network properties is shown.

The paper is structured as follows. In Sect. 2, the pore-network model is described, including the precipitation reaction. The different model concepts CAPs and CTs for simulating the precipitation in pore throats are introduced in Sect. 3. Section 4 shows the results of the comparison of the concepts. The results are discussed in Sect. 5 and final remarks are given in Sect. 6.

2 Pore-Network Model

In this section the pore-network model for saturated flow is described, including the mathematical model in Sect. 2.1, the chemical reaction in Sect. 2.2 and the numerical model in Sect. 2.3.

2.1 Mathematical Model

In this paper, the pore-network model presented in Weishaupt et al. (2019) is used and expanded to model salt precipitation, see Fig. 1. A one-phase, multi-component fluid system is considered. The fluid consists of the components water and NaCl. Additionally, a solid phase represents the precipitated NaCl. For the simulations in this paper,

solution-dependent fluid properties from Jambhekar et al. (2015) are used. Density as well as viscosity of the saline solution are functions of pressure, salt concentration and temperature. The model is non-isothermal, but the influence of temperature is of minor importance in the considered problem. Therefore, the used energy balance is not introduced here, but for details it is referred to Weishaupt et al. (2022).

The balance equation is solved in every pore body for each component κ, using the primary variables liquid pressure p, salt mole fraction x^{NaCl} and precipitated salt volume fraction ϕ_{s}.

$$\begin{aligned}\frac{\mathrm{d}(V_i \rho_{\mathrm{m},i} x_i^\kappa)}{\mathrm{d}t} &= \sum_{j=1}^{N} Q_{ij} \left(\rho_{\mathrm{m}} x^\kappa\right)_{\mathrm{up}} \\ &\quad + \sum_{j=1}^{N} D_{\mathrm{m}} A_{ij} \frac{\rho_{\mathrm{m},j} x_j^\kappa - \rho_{\mathrm{m},i} x_i^\kappa}{l_{ij}} + s_i^\kappa \qquad \kappa \in \{\mathrm{w}, \mathrm{NaCl}\}.\end{aligned} \tag{1}$$

Here V_i describes the volume of pore body i, Q_{ij} the in- or outgoing volume flux from pore throat ij and ρ_{m} the molar density of the fluid. For the advective fluxes, the concentration $\left(\rho_{\mathrm{m}} x^\kappa\right)_{\mathrm{up}}$ of the upstream pore body is used. Further, D_{m} is the molecular diffusion coefficient and A_{ij} and l_{ij} are the cross-sectional area and length of the pore throat between pore body i and j. The change in amount of moles in every pore body i (storage term on the left-hand side) is calculated by the sum of the advective fluxes of every pore-throat connected to the pore-body (first term on the right-hand side). Further the diffusive fluxes between the neighbouring pore bodies are considered (second term) as well as a reaction term s_i^κ, which is specified in Sect. 2.2 for NaCl and is zero for water. The mole fraction of water x^{w} is defined by the closure relationship $x^{\mathrm{w}} + x^{\mathrm{NaCl}} = 1$. For the solid phase, the mass balance reduces to the following equation:

$$V_{\mathrm{ini},i} \rho_{\mathrm{m,s}} \frac{\mathrm{d}\phi_{\mathrm{s},i}}{\mathrm{d}t} = s_{\mathrm{s},i}^{\mathrm{NaCl}}. \tag{2}$$

Here $\rho_{\mathrm{m,s}}$ is the molar density of the solid salt and $\phi_{\mathrm{s},i}$ the solid volume fraction in pore body i, which describes the precipitated volume over the initial pore-body volume $V_{\mathrm{ini},i}$. A change in mass of solid salt is only caused by dissolution or precipitation described by the reaction term $s_{\mathrm{s},i}^{\mathrm{NaCl}}$.

The flow in the pore throat is calculated by a Hagen–Poiseuille equation. The flow resistance in the pore bodies is neglected. The volume flux Q_{ij} depends on the pressure difference $p_j - p_i$ between pore body i and j:

$$Q_{ij} = g_{ij}(p_j - p_i). \tag{3}$$

The transmissibility g_{ij} describes the flow resistance of the pore throat and depends on the pore-throat geometry. The transmissibility of the throats determines the overall flow behaviour of the pore-network system and thus is an important parameter. Different concepts for the transmissibility calculation (CTs) for pore throats are presented in Sect. 3.2.

The actual volume V_i is the initial pore-body volume $V_{\mathrm{ini},i}$ decreased by the volume occupied by the solid salt:

$$V_i = V_{\mathrm{ini},i}(1 - \phi_{\mathrm{s},i}). \tag{4}$$

2.2 Chemical Reaction

A kinetic reaction is used for the description of the precipitation of NaCl in the pore bodies. The concepts to determine the amount precipitating in the throats are presented in Sect. 3.1. The kinetic reaction rate s_i^{NaCl} in each pore body is calculated as follows:

$$s_i^{\mathrm{NaCl}} = -s_{\mathrm{s},i}^{\mathrm{NaCl}} = -kA_{\mathrm{react},i}(\Omega - 1). \tag{5}$$

Here the reaction constant $k = 10^{-3}$ mol/(m^{2}s) is used (Mejri et al. 2017; Jambhekar et al. 2016). The reactive surface $A_{\mathrm{react},i}$ is the surface area of the pore body, which is based on the pore-body dimensions and geometry. The saturation index Ω describes the salt saturation of the solution:

$$\Omega = \frac{IAP}{K_{\mathrm{eq}}^{\mathrm{NaCl}}} = \frac{[\mathrm{Na}^+][\mathrm{Cl}^-]}{K_{\mathrm{eq}}^{\mathrm{NaCl}}}, \tag{6}$$

where IAP is the ionic activity product, which is the product of the activities of the dissolved ions $[ion]$ in the solution. Further, $K_{\mathrm{eq}}^{\mathrm{NaCl}}$ is the equilibrium constant, which is the product of the activities at the solubility limit. For $\Omega > 1$ the solution is oversaturated, for $\Omega = 1$ saturated and for $\Omega < 1$ undersaturated. To calculate the IAP the activities of the ions Na^+ and Cl^-, a simplified Pitzer approach presented in Pérez-Villaseñor et al. (2002) is used. It is assumed that the ions have an equal concentration in the solution thus NaCl can be considered as one component for the mass transport. The equilibrium constant $K_{\mathrm{eq}}^{\mathrm{NaCl}}$ is calculated as well using the following Pitzer approach. For the molality $m_{\mathrm{eq}} = 6.14$ molNaCl/kg$\mathrm{H_2O}$ (Pérez-Villaseñor et al. 2002) at the solubility limit of NaCl this leads to $K_{\mathrm{eq}}^{\mathrm{NaCl}} = 38.0464$. For the activity of the ions $[ion]$, it follows:

$$[ion] = \gamma^{ion}\frac{m^{ion}}{m_0} \qquad ion \in \{\mathrm{Na}^+, \mathrm{Cl}^-\}, \tag{7}$$

where the molality at the standard state is $m_0 = 1$ mol NaCl/kg $\mathrm{H_2O}$. The molality of the ion m^{ion}, which can be calculated from the mole fractions and the molar mass of water M^{w}, is

$$m = m^{\mathrm{NaCl}} = m^{\mathrm{Na}^+} = m^{\mathrm{Cl}^-} = \frac{x^{\mathrm{NaCl}}}{x^{\mathrm{w}} \cdot M^{\mathrm{w}}}. \tag{8}$$

The activity coefficient γ^{ion} is calculated using the simplified Pitzer approach presented in Pérez-Villaseñor et al. (2002). The approach calculates the activity coefficient for electrolytes with the form $X_{y+}^{u+}Y_{y-}^{u-}$ where X is the cation and Y the anion. For NaCl, X corresponds to Na and Y to Cl. The equation presented in Pérez-Villaseñor et al. (2002) simplifies in the case of NaCl as the protonic units are $u^{\mathrm{Na}^+} = u^{\mathrm{Cl}^-} = 1$ and the number of ions are $y^{\mathrm{Na}^+} = y^{\mathrm{Cl}^-} = 1$. For NaCl it follows:

$$\begin{aligned}\ln(\gamma^{\mathrm{Na}^+}) = \ln(\gamma^{\mathrm{Cl}^-}) = -A_\phi\left(\frac{\sqrt{I}}{1+b\sqrt{I}} + \frac{2}{b}(1+b\sqrt{I})\right) \\ + \frac{4}{y}m\beta^{\mathrm{NaCl}} + \frac{6}{y}m^2C^{\mathrm{NaCl}}.\end{aligned} \tag{9}$$

Here I is the ionic strength of NaCl:

$$I = \frac{1}{2} \sum_{ion} (u^{ion})^2 \frac{m^{ion}}{m_0} = m. \tag{10}$$

The further used parameters for NaCl are described in Table 1.

2.3 Numerical Model

The pore-network model is implemented in DuMu^X (Koch et al. 2018, 2020), an open-source simulator for multi-phase flow and multi-component transport in porous media. DuMu^X is based on Dune (Bastian et al. 2021), a toolbox for solving partial differential equations.

A first-order backward Euler scheme is used for the temporal discretization. The Newton method is used to linearize the system of equations at every time step. All balance equations are assembled in one system of equations, which is solved simultaneously for all primary variables.

If the volume of an individual pore body or throat is 98% filled with precipitated salt, the pore body or pore throat is assumed to be completely blocked. In this case the simulation aborts to avoid problems in numerical convergence. A higher termination criterion would be possible, but a longer simulation time would not bring any new insights.

3 Model Concepts for Precipitation in Pore Throats

This section presents the different concepts to model salt precipitation in pore throats. The concepts for the amount of precipitation (CAPs) are presented in Sect. 3.1. These concepts calculate the amount of precipitate in the throats and thus determine the current volume of the throat. The concepts for the transmissibility (CTs) are presented in Sect. 3.2. These concepts use the volume of the throat determined by the CAPs as input parameter to calculate the pore-throat transmissibility. The concepts of both types can be combined arbitrarily. An overview of all CAPs and CTs and their connection through the respective in- and output variables is shown in Fig. 2. Further details of the implementation are presented in Appendix A in form of a flow chart, see Fig. 14.

In this paper we restrict ourselves to circular (Fig. 1) and rectangular (Fig. 2) cross-sectional shapes for the pore throats. But most of the concepts can be transferred to other shapes. Further, spherical pore-bodies are used in all setups in the paper. However, the throat concepts are not limited to a certain pore-body geometry. Only the formulation of

Table 1 Parameters for the calculation of the activity coefficient using the Pitzer approach

Parameter	Value	Description
$y = y^{Cl^-} + y^{Na^+}$	2	Sum of ions
A_ϕ	0.39159[1]	Debye–Hückel constant at 298.15 K
b	2.22718 $\sqrt{\text{kg/mol}}$[1]	Characteristic constant
β^{NaCl}	0.05383[1]	NaCl specific coefficient for Pitzer approach
C^{NaCl}	0.00134[1]	NaCl specific coefficient for Pitzer approach

[1]Source: Pérez-Villaseñor et al. (2002)

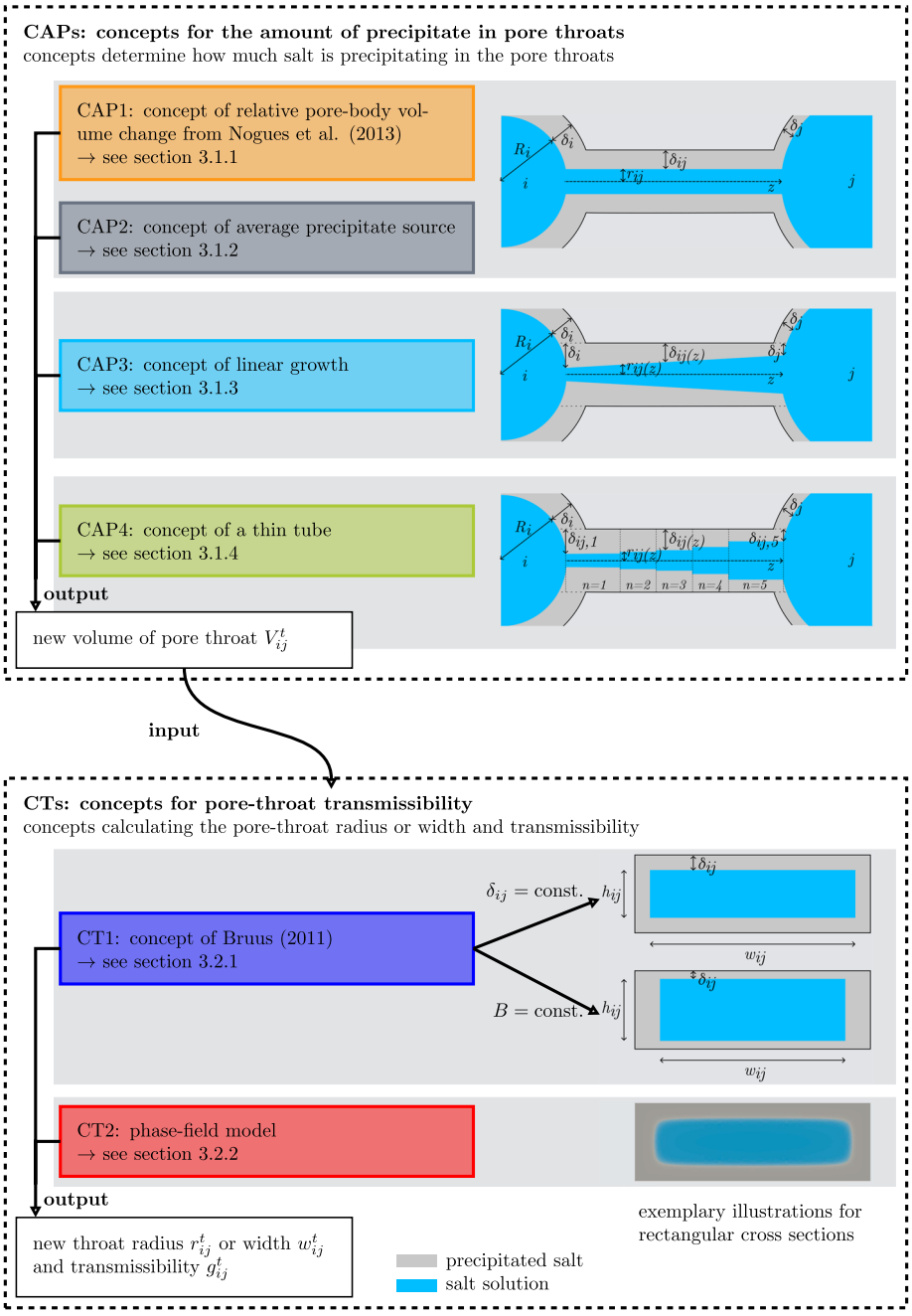

Fig. 2 Overview over the different concepts presented in this paper

CAP3 is specific for a pore-body geometry. In this paper, CAP3 is developed for spherical pore-bodies, but can easily transferred to other pore-body geometries.

3.1 CAPs: Concepts for the Amount of Precipitate in Pore Throats

Four different concepts are used to calculate the volume of precipitate in the throat. The concepts differ in the assumption on how the precipitated salt is distributed along the throat, see Fig. 2. CAP1 and CAP2 assume a constant precipitation layer thickness, CAP3 a linear distribution along the throat and for CAP4 the distribution is variable. Further, different information of the adjacent pore bodies is used to calculate the amount of precipitation in the throat and the resulting throat volume.

The first concept (CAP1) is taken from Nogues et al. (2013), CAP2 and CAP3 are developed in this paper and CAP4 is based on ideas from van Noorden (2009), Kumar et al. (2011) and Bringedal et al. (2016) and adapted for use in the pore-network model.

For the first three concepts (CAP1-CAP3), the volume of the throats is considered by adding it to the pore-body volume. This volume is used in the storage term of the mole balance (Eqs. (1) and (2)) and affects the reactive surface $A_{\mathrm{react},i}$ in the precipitation reaction. To calculate the volume of precipitation in the throat, the throat volume is used separately. But this precipitated volume in the throats does not appear in the mole balance and it is only used to calculate the new throat transmissibility. CAP4 differs fundamentally from the first three, as it uses mole balance equations along the pore throat, in which it is accounted for the throat volume separately. They are obtained by using asymptotic methods and transversal averaging and are then coupled with the ones in the pore bodies. In the numerical modelling, the equations along the pore throat are discretized, providing a pore-network model that includes unknowns attached to the pore throats.

3.1.1 CAP1: Concept of Relative Pore-Body Volume Change from Nogues et al. (2013)

Nogues et al. (2013) developed a pore-network model to investigate permeability-porosity relationships on the REV-scale for conditions of geological CO_2-sequestration. The precipitation and dissolution of different carbonate species due to flow of CO2-rich waters under high pressure conditions is considered. The concept for the change in throat radius in this paper is based on the assumption of a correlation between pore-throat radius and the volume of the adjacent pore bodies. The underlying concept is used to construct pore networks and presented in Li et al. (2006). It assumes that the throat transmissibility is correlated to the sum of the logarithm of the adjacent pore-body volumes. This assumption is based on experimental investigations of correlation of the pore-throat and pore-body structures of sand stones. Consequently, CAP1 is based on the analysis of existing pore structures and not on assumptions regarding the precipitation process and resulting change in pore space.

The concept calculates one constant reduced diameter for each pore throat, see Fig. 2. In Nogues et al. (2013), the following relationship for circular pore-throat cross sections is given:

$$r_{ij}^{t} = r_{ij}^{t-1} + r_{ij}^{t-1} \cdot \left(\frac{V_i^t - V_i^{t-1}}{V_i^{t-1}} + \frac{V_j^t - V_j^{t-1}}{V_j^{t-1}} \right) \tag{11}$$

$$= r_{ij}^{t-1} \cdot \left(\frac{V_i^t}{V_i^{t-1}} + \frac{V_j^t}{V_j^{t-1}} - 1 \right). \tag{12}$$

Here, r_{ij}^{t-1} describes the throat radius and V_i^{t-1} the volume of the previous time step, and r_{ij}^t and V_i^t are the respective parameters for the current time step. Note that this concept is only valid for circular cross sections. The change in throat volume $\Delta V_{ij}^{\Delta t}$ and new volume of the pore throat V_{ij}^t can be calculated as follows:

$$\Delta V_{ij}^{\Delta t} = \pi l_{ij} \left(\left(r^t \right)^2 - \left(r^{t-1} \right)^2 \right), \tag{13}$$

$$V_{ij}^t = V_{ij}^{t-1} + \Delta V_{ij}^{\Delta t}. \tag{14}$$

3.1.2 CAP2: Concept of Average Precipitate Source

The idea of CAP2 is that the throat volume changes based on the source terms $s_{s,i}^{\mathrm{NaCl}}$ of the adjacent pore bodies:

$$\Delta V_{ij}^{\Delta t} = \frac{1}{2} \left(\frac{s_{s,i}^{\mathrm{NaCl},t-1}}{V_i^{t-1}} + \frac{s_{s,j}^{\mathrm{NaCl},t-1}}{V_j^{t-1}} \right) \cdot \frac{V_{ij}^{t-1} \cdot \Delta t}{\rho_{m,s}^{t-1}}, \tag{15}$$

$$V_{ij}^t = V_{ij}^{t-1} + \Delta V_{ij}^{\Delta t}. \tag{16}$$

The source term, defined in Eq. (5), describes the amount of salt molecules in mole per time precipitating from the saline solution. The calculation of the source terms for the adjacent pore bodies is based on the salt mole fraction in the respective pore bodies. In this concept the source terms of the neighbouring pore bodies are normalized with their respective volume and averaged arithmetically to estimate a source term for the pore throat. This averaged source term is then multiplied with the volume of the throat and the current time step size to get the amount of salt molecules precipitating in the throat. With the molar solid salt density $\rho_{m,s}$, the change in throat volume can be calculated. We assume a constant distribution of the precipitated salt along the throat, see Fig. 2. This concept can be applied to different cross-sectional shapes as e.g. circular or rectangular ones.

3.1.3 CAP3: Concept of Linear Growth

CAP3 uses different dimensions of the pore-throat cross-section at each end of a pore throat. We assume that the ends of the pore throats experience the same precipitation rate as their connected pore bodies, and therefore obtain the same thickness of precipitated layer at the ends. Between the two throat ends a linear behaviour of the pore-throat dimensions is assumed, see Fig. 2. In the following we derive the approach for spherical pore bodies, but it can be adapted easily for other shapes. The change in pore-body radius $\Delta R_i^{\Delta t}$ during time step Δt is therefore given by:

$$\Delta R_i^{\Delta t} = \left(\frac{3}{4\pi} \right)^{1/3} \left(\left(V_i^t \right)^{1/3} - \left(V_i^{t-1} \right)^{1/3} \right). \tag{17}$$

For circular throat cross sections, the throat radius r_i adjacent to pore body i and the throat radius $r(z)$ depending on the z-coordinate along the throat are given by the following relations:

$$r_i^t = r_i^{t-1} + \Delta R_i^{\Delta t}, \tag{18}$$

$$r(z) = r_i + \frac{r_j - r_i}{z_j - z_i} z. \tag{19}$$

The linear relationship is integrated along the throat and inserted in Eq. (46) for the volume flow from CT1, which is presented in Sect. 3.2.1. The following formulation is obtained for circular throat cross sections:

$$Q_{ij} = \frac{\pi r^4}{8\mu} \frac{\partial p}{\partial z} \tag{20}$$

$$= \frac{\pi}{8\mu} \frac{1}{\int_{z_i}^{z_j} \frac{1}{r^4} dz} (p_j - p_i) \tag{21}$$

$$= \frac{\pi}{8\mu l_{ij}} \frac{3 r_i^3 r_j^3}{r_i^2 + r_i r_j + r_j^2} (p_j - p_i). \tag{22}$$

With the same approach also relations for further cross-sectional shapes can be derived. For rectangular throat cross sections, the following assumptions are used in this concept: The area of the cross section reduces as if salt precipitates in an equal thick layer, using the thickness of the salt layer in the adjacent pore body. However, it is assumed that the aspect ratio $B = \frac{h}{w}$ of the cross section stays constant for the calculation of the height and width of the throat cross section, where $h < w$. The derivation of the following, resulting relation can be found in Appendix B:

$$h_i^t = \sqrt{h_i^{t-1} + 2\Delta R_i^{\Delta t}} \sqrt{h_i^{t-1} + 2B\Delta R_i^{\Delta t}}, \tag{23}$$

$$h(z) = h_i + \frac{h_j - h_i}{z_j - z_i} z. \tag{24}$$

The following relation is obtained for rectangular cross sections using Eq. (47) from the CT1:

$$Q_{ij} = \frac{1}{12\mu} h^3 w (1 - 0.63B) \frac{\partial p}{\partial z} \tag{25}$$

$$= \frac{1}{12\mu} \frac{1}{\int_{z_i}^{z_j} \frac{1}{h^3 w (1 - 0.63B)} dz} (p_j - p_i) \tag{26}$$

$$= \frac{1}{12\mu l_{ij}} \frac{1 - 0.63B}{B} \frac{3 h_i^3 h_j^3}{h_i^2 + h_i h_j + h_j^2} (p_j - p_i). \tag{27}$$

Equations (22) and (27) correspond to the formulations from Bruus (2011) (Eqs. (46) and (47)) using an effective radius or height:

$$r_{ij,\mathrm{eff}} = \left(\frac{3 r_i^3 r_j^3}{r_i^2 + r_i r_j + r_j^2} \right)^{1/4}, \tag{28}$$

$$h_{ij,\mathrm{eff}} = \left(\frac{3 h_i^3 h_j^3}{h_i^2 + h_i h_j + h_j^2} \right)^{1/4}. \tag{29}$$

The volume of the pore throat can be calculated using the effective quantities. For circular or rectangular throat cross section, the volume is:

$$V_{ij,\mathrm{circ}} = \pi l_{ij} r_{ij,\mathrm{eff}}^2, \tag{30}$$

$$V_{ij,\mathrm{rect}} = \frac{l_{ij}}{B} h_{ij,\mathrm{eff}}^2. \tag{31}$$

3.1.4 CAP4: Concept of a Thin Tube

Instead of assuming a certain distribution of the precipitate at the pore walls, this concept uses transversally averaged balance equations along pore throats. These are derived in van Noorden (2009), Kumar et al. (2011) and Bringedal et al. (2016) for thin strips, by employing asymptotic expansion methods. The derivation can be transferred to thin tubes assuming axial symmetry. This leads to one-dimensional pore-throat models, in which the relevant quantities are averaged over the throat cross-section. In this section, the variables depending on all three dimensions x, y and z are denoted with a tilde $\tilde{x}$ and the variables averaged over x and y and consequently depending only on z are denoted with a bar $\bar{x}$. The averaged mole fraction $\bar{x}_{ij}^{\kappa}$ and the averaged molar density $\bar{\rho}_{\mathrm{m},ij}^{\kappa}$ are derived by integrating over the throat cross section:

$$\bar{x}_{ij}^{\kappa}(t,z) = \frac{1}{A_{ij}} \int_{A_{ij}} \tilde{x}_{ij}^{\kappa}(t,x,y,z)\,\mathrm{d}x\mathrm{d}y, \tag{32}$$

$$\bar{\rho}_{\mathrm{m},ij}(t,z) = \frac{1}{A_{ij}} \int_{A_{ij}} \tilde{\rho}_{\mathrm{m},ij}(t,x,y,z)\,\mathrm{d}x\mathrm{d}y. \tag{33}$$

As the source term is dependent on $\bar{x}_{ij}^{\mathrm{NaCl}}$ it becomes also an averaged parameter $\bar{s}_{ij}^{\kappa}$. Per definition, the solid volume fraction $\phi_{s,ij}$ is a parameter averaged over the throat cross section. For the averaged mole balance it follows:

$$\partial_t \left(A_{ij} \bar{\rho}_{\mathrm{m},ij} \bar{x}_{ij}^{\kappa} \right) = \partial_z \left(A_{ij} \left(\bar{\rho}_{\mathrm{m},ij} \bar{x}_{ij}^{\kappa} Q_{ij} + D_{\mathrm{m}} \partial_z \left(\bar{\rho}_{\mathrm{m},ij} \bar{x}_{ij}^{\kappa} \right) \right) \right) + \bar{s}_{ij}^{\kappa}, \tag{34}$$

$$A_{\mathrm{ini},ij}\rho_{\mathrm{m,s}}\partial_t\left(\phi_{s,ij}\right) = -\bar{s}_{ij}^{\mathrm{NaCl}}. \tag{35}$$

The throat is discretized along the throat in z-direction to solve Eqs. (34) and (35), see Fig. 2. Information about the primary variables along the throat are gained and the reaction term can be solved for every discretized throat section n:

$$\begin{aligned}\frac{\mathrm{d}(V_{ij,n}\bar{\rho}_{\mathrm{m},ij,n}\bar{x}_{ij,n}^{\kappa})}{\mathrm{d}t} &= Q_{ij,\mathrm{up}}\bar{\rho}_{\mathrm{m},ij,\mathrm{up}}\bar{x}_{ij,\mathrm{up}}^{\kappa} + Q_{ij,n}\bar{\rho}_{\mathrm{m,ij,n}}\bar{x}_{ij,n}^{\kappa} \\ &+ D_{\mathrm{m}}A_{ij,z,z+1}\frac{\bar{\rho}_{\mathrm{m},ij,n-1}\bar{x}_{ij,n-1}^{\kappa} - \bar{\rho}_{\mathrm{m},ij,n}\bar{x}_{ij,n}^{\kappa}}{\Delta l_{ij,\mathrm{n,n-1}}} \\ &+ D_{\mathrm{m}}A_{ij,z,z+1}\frac{\bar{\rho}_{\mathrm{m},ij,n+1}\bar{x}_{ij,n+1}^{\kappa} - \bar{\rho}_{\mathrm{m},ij,n}\bar{x}_{ij,n}^{\kappa}}{\Delta l_{ij\mathrm{n,n+1}}} \\ &+ \bar{s}_{ij,n}^{\kappa},\end{aligned} \tag{36}$$

$$V_{\mathrm{ini},ij,n}\rho_{\mathrm{m,s}}\frac{\mathrm{d}\phi_{\mathrm{s},ij,n}}{\mathrm{d}t} = \bar{s}_{\mathrm{s},ij,n}^{\mathrm{NaCl}}, \tag{37}$$

where the subscript up describes the upstream throat section of n. For the advective flux, Eq. (3) is used in the form:

$$Q_{ij} = g_{ij,n,n\pm1}(p_{ij,n\pm1} - p_{ij,n}). \tag{38}$$

A diffusive flux between the single throat sections is calculated using the salt concentration differences between the throat sections. With this concept we can resolve the salt concentration and the volume fraction of precipitated salt along the throat. And consequently the new volume of the pore-throat sections can be calculated.

Equations (36) and (37) equal the form of the mole balance equations (1) and (2) for the pore bodies in the general pore-network model. For the implementation, the existing pore-network model structure can be used. So-called pseudo pore bodies are introduced along the throat for each throat section. They are characterized by only one incoming and one outgoing pore throat. The volume of each pseudo pore body equals the one of the corresponding throat section. In this concept the throat volume is not considered in the pore-body volumes. For these pseudo pore bodies the same mole balance equations (Eqs. (1) and (2)) as for the main pore bodies are used, which then reduce to the above derived equations (Eqs. (36) and (37)). The change in volume in the pseudo pore bodies is then transferred to the respective throat sections. Based on that, a new throat radius for the respective throat section can be calculated. The source term (Eq. (5)) uses the reactive surface of the pseudo pore body for simplicity. For a detailed description of the implementation, it is referred to Appendix C.

3.2 CTs: Concepts for Pore-Throat Transmissibility

Two different concepts are used to calculate the transmissibility of the pore throats for a given volume. The two concepts differ in the assumption on how the salt is distributed within the throat cross section, see Fig. 2. First we use a widely used concept introduced by Bruus (2011) (CT1), which relies on an explicit form of the domain occupied by solid salt. Second we use the solution of a classical reactive Cahn–Hilliard evolution

equation (see Cahn and Hilliard 1958) (CT2), called phase-field model in the sequel. It accounts for the chemical reaction and determines the precipitate's cross-sectional distribution by minimizing the interfacial area between solid and fluid phase. This concept works for arbitrary cross-sectional shape, but comes with considerably higher numerical complexity.

The volume of precipitated salt in the throat and the consequent pore throat volume are determined by the approaches in the previous Sect. 3.1. From the volume of the pore throat, the dimensions of the throat cross sections are calculated for the different cross-sectional shapes. For CT2 the cross-sectional area A_{ij}^t is used as input for the phase-field model:

$$A_{ij}^t = \frac{V_{ij}^t}{l_{ij}}. \tag{39}$$

The relations of CT1 depend on the radius or width and height of the throat. The following then applies to the radius of a circular throat cross section:

$$r_{ij}^t = \sqrt{\frac{V_{ij}^t}{\pi l_{ij}}}. \tag{40}$$

For the rectangular cross-sectional shape two different assumptions are used in case of CT1 for most of the CAPs. On the one hand it is assumed that the aspect ratio $B = h/w$ of the rectangle stays constant with the precipitation of the salt. On the other hand it is assumed that the salt precipitates in a layer of constant thickness δ at the throat wall, see Fig. 2. For rectangular cross sections using the assumption of a constant aspect ratio ($B = \text{const.}$), it follows for the width and height:

$$w_{ij}^t = \sqrt{\frac{V_{ij}^t}{B l_{ij}}}, \tag{41}$$

$$h_{ij}^t = B w_{ij}^t. \tag{42}$$

A quadratic equation results for rectangular cross sections using the assumption of an equal thick precipitation layer ($\Delta\delta_{ij} = \text{const.}$):

$$l_{ij}\left(w_{ij}^t\right)^2 + \left(h_{\text{ini}} - w_{\text{ini}}\right) l_{ij} w_{ij}^t - V_{ij}^t = 0. \tag{43}$$

This results in the following for the width and height:

$$w_{ij}^t = \frac{-\left(h_{\text{ini}} - w_{\text{ini}}\right) l_{ij} + \sqrt{\left(\left(h_{\text{ini}} - w_{\text{ini}}\right) l_{ij}\right)^2 + 4 l_{ij} V_{ij}^t}}{2 l_{ij}}, \tag{44}$$

$$h_{ij}^t = \frac{V_{ij}^t}{l_{ij} w_{ij}^t}. \tag{45}$$

3.2.1 CT1: Concept of Bruus (2011)

Bruus (2011) presents relations for volume flow through tubes with different cross-sectional shapes. The derivation is based on the integration of the one-dimensional stationary Stokes equations over the cross-section area using the assumption of no-slip at the throat walls. With that the following relations for the volume flux Q_{ij} and transmissibility g_{ij} of the pore throat are obtained as a specification of Eq. (3). For circular and rectangular cross-sectional shapes we get, respectively:

$$\text{circular}: \; Q_{ij} = \underbrace{\frac{\pi}{8\mu_{\text{up}} l_{ij}} r_{ij}^4}_{g_{\text{circ},ij}} \left(p_j - p_i\right), \tag{46}$$

$$\text{rectangular}: \; Q_{ij} = \underbrace{\frac{1}{12\mu_{\text{up}} l_{ij}} h_{ij}^3 w_{ij} \left(1 - 0.63 \frac{h_{ij}}{w_{ij}}\right)}_{g_{\text{rect},ij}} \left(p_j - p_i\right) \quad \text{for } h_{ij} < w_{ij}. \tag{47}$$

Here μ_{up} describes the viscosity of the fluid in the upstream pore body. In both relations, the transmissibility decreases if the radius r_{ij} or height h_{ij} and width w_{ij} of the throat cross section decreases due to precipitation of salt.

3.2.2 CT2: Phase-Field Model

As a second concept we use a geometric evolution equation governing the precipitation process. The solution of this reactive Cahn–Hilliard equation (the phase-field model) is used to calculate the resulting transmissibility of pore throats. Therefore, the pore-network model is coupled with the phase-field model. In each time step, first the pore-network model is solved and the amount of salt precipitated in the individual throats is calculated based on the CAPs from Sect. 3.1. With this information, the phase-field model is run for every pore throat until the determined amount of precipitation from the pore-network model is reached. The phase-field model calculates the precipitate distribution and transmissibility of the throat, which is afterwards used in the pore-network model.

The phase-field model provides the evolution of the precipitate indicator variable $\phi \in [0, 1]$. We interpret $\phi = 0$ as complete solid state and $\phi = 1$ as fluid state. In fact, we consider a geometric evolution equation of Cahn–Hilliard type which belongs to the class of diffuse-interface models: the fluid-solid interface is represented as a smooth transition of ϕ from 0 to 1 over the width of the order of the given phase-field parameter ϵ.

We assume that the throat cross-sectional shape does not depend on its position along the pore throat and that the velocity v_z is perpendicular to the cross-section (see Rohde and Von Wolff 2021; von Wolff et al. 2021; von Wolff and Pop 2022 for a fully coupled, reactive Navier–Stokes Cahn–Hilliard system). This means that the simulation of one cross-section is sufficient. In the following we present the phase-field model in a non-dimensional form, and emphasize the dependence of the transmissibility on dimensional quantities in (52).

For the evolution of the full precipitation process by phase-field modelling we refer to Rohde and Von Wolff (2021), von Wolff and Pop (2022), Bringedal et al. (2020). Under the

named assumptions on the flow field, the evolution of ϕ in Rohde and Von Wolff (2021) decouples from the flow dynamics and reduces to a reactive Cahn–Hilliard equation in the pore throat cross-section, that is

$$\partial_t \phi - \nabla \cdot (M\varepsilon \nabla \mu_c) = q(\phi)\mathcal{R}, \tag{48}$$

$$\mu_c = \frac{W'(\phi)}{\varepsilon} - \varepsilon \Delta \phi. \tag{49}$$

Here M is the constant mobility describing the time scale of evolution, $q(\phi) = \phi(1-\phi)$ is a function to locate the precipitation reaction which is only active at the fluid-solid interface, $\mathcal{R}$ is the constant precipitation rate, μ_c describes the chemical potential and $W(\phi) = \phi^2(1-\phi)^2$ is a double well function that drives the separation of phases. We solve for ϕ and μ_c in the non-dimensional unit square $\Omega = [0,1]^2$. We augment (48) by initial data and homogeneous Neumann boundary data for ϕ and μ_c.

The phase-field model is computed up to the time when the amount of salt has been precipitated, which is determined by one of the CAPs and provided as input for CT2. Then, the non-dimensional transmissibility $\hat{g}_{ij}$ is determined by calculating the non-dimensional flow profile followed by the integration over the cross-sectional area:

$$d(\phi)v_z - \nabla^2 v_z = \phi, \tag{50}$$

$$\hat{g}_{ij} = \int_\Omega v_z \, \mathrm{d}x\mathrm{d}y. \tag{51}$$

In the linear Eq. (50), the quantity v_z is the non-dimensional longitudinal velocity of the throat in Ω. It is set to zero on the boundary of Ω. The smooth interpolation function $d(\phi)$ with $d(1) = 0$ and $d(0) > 0$ determines the slip length realizing Navier-slip conditions at the fluid-solid interface in the sharp interface limit $\varepsilon \to 0$, see Rohde and Von Wolff (2021) for details.

With the reference side length h_{ref} for the non-dimensional unit square Ω, the following dimensional transmissibility can then be calculated in the pore-network model using the upstream viscosity μ_{up}:

$$g_{ij} = \frac{h_{\text{ref}}^4}{l_{ij}\mu_{\text{up}}} \hat{g}_{ij}. \tag{52}$$

Based on the phase-field calculation, the cross-sectional shape can alter due to the precipitation, especially for rectangular, elliptical or arbitrary cross sections, see Fig. 2. In addition, the phase-field concept can be applied to arbitrary cross-sectional shapes.

The phase-field model is computationally more expensive than the use of the relations of Bruus (2011). To overcome this disadvantage, also analytical relations for specific cross-sectional shapes can be generated for the transmissibility of the throat using the phase-field model. The phase-field model simulates the precipitation in the throat until it is fully clogged. The obtained relationship of the cross-sectional area and the transmissibility is then approximated with a polynomial. These relations are restricted to the specific cross-sectional shapes they are generated for, and are only valid for the case of precipitation absent of interruptions with dissolution phases. The following relations are obtained for initially circular and rectangular throat cross sections with $B = \frac{1}{3}$.

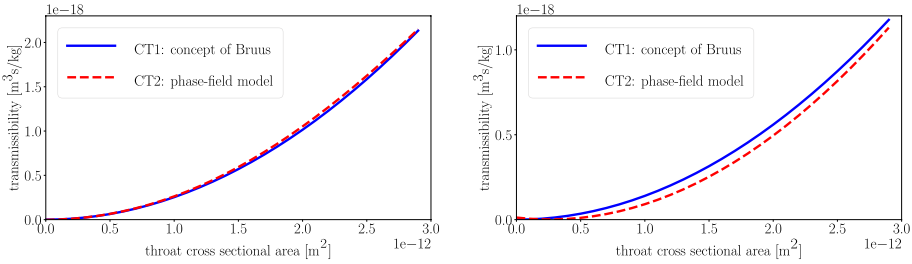

(a) Circular throat cross section. (b) Rectangular throat cross section.

Fig. 3 Relationship of cross-sectional area and transmissibility of the pore throat calculated with the equations of Bruus (2011) (CT1) and the phase-field model (CT2)

$$\begin{aligned}\hat{g}_{\mathrm{circ},ij} = &-3.604331 \cdot 10^{-4} + 1.701298 \cdot 10^{-3}\hat{A}_{ij} + 3.748056 \cdot 10^{-2}\hat{A}_{ij}^2 \\ &+ 3.272596 \cdot 10^{-3}\hat{A}_{ij}^3 - 8.834939 \cdot 10^{-4}\hat{A}_{ij}^4,\end{aligned} \tag{53}$$

$$\begin{aligned}\hat{g}_{\mathrm{rect},ij} = &\ 1.917621 \cdot 10^{-3} - 1.342814 \cdot 10^{-2}\hat{A}_{ij} + 2.585258 \cdot 10^{-2}\hat{A}_{ij}^2 \\ &- 5.040701 \cdot 10^{-5}\hat{A}_{ij}^3 - 2.570248 \cdot 10^{-5}\hat{A}_{ij}^4.\end{aligned} \tag{54}$$

A non-dimensional throat cross-sectional area $\hat{A}_{ij} = \frac{A_{ij}}{h_{\mathrm{ref}}^2}$ and $h_{\mathrm{ref}} = 1\mu\mathrm{m}$ are used. These relations are plotted in Fig. 3 and compared to the relations of Bruus (2011). Only small differences arise between the two CTs, which are mainly based on the different assumptions of the distribution of the precipitated salt. For detailed discussion of the CTs, see section 5.2.

4 Results

Different comparisons of the throat concepts are presented in the following sections. First, in Sect. 4.1 the used setups and the evaluation values are presented. In Sect. 4.2 the CAPs are compared. Section 4.3 contains the investigation of the influence of the number of throat sections in CAP4. The CTs are compared in Sect. 4.4.

4.1 Simulation Setup and Evaluation

The different CAPs and CTs are applied using three different cases. A one-dimensional setup with two different cases of boundary and initial conditions, see Sect. 4.1.1 and a two-dimensional case, see Sect. 4.1.2. To compare the concepts, global parameters of the pore-network like the permeability and the distribution of precipitated salt are evaluated as described in Sect. 4.1.3.

4.1.1 One-Dimensional Cases

The one-dimensional setup consists of five equally sized, spherical pore bodies that are arranged in a row and connected by four equally sized pore throats, see Fig. 4. The

initial dimensions are listed in Table 2. Circular and rectangular cross-sectional shapes are considered for the pore throats, which have the same size of cross-sectional area initially.

Two different cases with different initial and boundary conditions are considered. For both cases, the same constant total molar flux is applied to the outlet pore body ($i = 4$) as a Neumann boundary condition, while a Dirichlet boundary condition is used for the inlet pore body ($i = 0$). In both cases, no precipitated salt is present initially and a constant temperature is applied.

In case 1, the system is initially filled with saturated saline solution. On the left-hand side, an oversaturated saline solution is injected. Additionally, an alternative higher molar flux is used in case 1 to investigate the influence of Q. In case 2, the system is initially filled with an oversaturated saline solution and a saturated saline solution enters the system at the inlet pore body. The specific values for both cases can be found in Table 3.

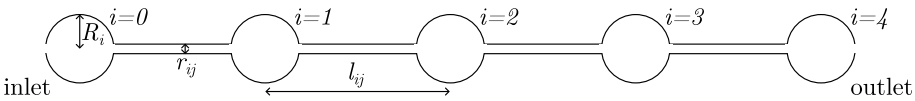

Fig. 4 One-dimensional setup of the pore-network system used to compare the different throat concepts. Five equally sized pore bodies in one row ($i = 0$ to $i = 4$) are connected with four equally sized pore throats ij. The dimensions can be found in Table 2

Table 2 Dimensions of the one-dimensional pore-network

Pore-network entity	Parameter	Size	Description
Pore bodies	R_i	1.0×10^{-5} m	Initial pore-body radius
Pore throats	l_{ij}	1.0×10^{-4} m	Pore-throat length
	A_{ij}	3.14×10^{-12} m	Initial cross-sectional area
	r_{ij}	1.0×10^{-6} m	Initial circular cross-sectional radius
	$B = \frac{h}{w}$	$\frac{1}{3}$	Initial rectangular cross-sectional height/width ratio

Table 3 Boundary and initial conditions of the one-dimensional setup

Case	Parameter	Size	Description
General	$p_0 = p_{\text{ini}}$	1.004×10^5 Pa	Initial and inlet pressure
	$\phi_{s,0} = \phi_{\text{s,ini}}$	0.0	Initial and inlet precipitated salt volume fraction
	$T_0 = T_{\text{ini}}$	293.15 K	Initial and inlet temperature
	$Q_{\text{m,4}}$	5×10^{-12} mol/s	Molar flux leaving outlet pore body
Case 1	$x_{\text{ini}}^{\text{NaCl}}$	0.0996 for $i > 0$	Initial salt mole fraction
		0.1 for $i = 0$	
	x_0^{NaCl}	0.1	Salt mole fraction at inlet pore body
	$Q_{\text{m,4,high}}$	5×10^{-11} mol/s	Alternative higher molar flux leaving outlet pore body
Case 2	$x_{\text{ini}}^{\text{NaCl}}$	0.15 for $i > 0$	Initial salt mole fraction
		0.0996 for $i = 0$	
	x_0^{NaCl}	0.0996	Salt mole fraction at inlet pore body

The time-step size is chosen so that it is smaller than the time needed for the fluid to pass one pore throat or throat section. For CAP4, smaller time-step sizes are needed than for the other concepts as the throat is divided in smaller throat sections.

The one-dimensional setup can be characterized by the dimensionless Peclet and Damköhler number. For the Peclet number it follows for initial conditions $\mathrm{Pe} = \frac{Q_{\mathrm{m},4} l_{ij}}{A_{ij} D_{\mathrm{m}} \rho_{\mathrm{m}}} = 24.3$, which indicates the domination of advective velocity over the diffusive velocity. The Damköhler number is initially $\mathrm{Da} = \frac{k A_{\mathrm{react},i} (\Omega - 1)}{Q_{\mathrm{m},4} x^{\mathrm{NaCl}}} = 0.041$. Thus, the advective-transport velocity is faster than the precipitation-reaction velocity and the precipitation is limited by the reaction velocity. For the higher $Q_{\mathrm{m,4,high}}$ it is $\mathrm{Pe} = 243.3$ and $\mathrm{Da} = 0.0041$.

4.1.2 Two-Dimensional Case

The two-dimensional setup has the dimensions of 5×10 pore bodies, see Fig. 5. They are connected with pore throats in horizontal and vertical direction, from which some throats are deleted randomly with a possibility of 30%. The network was constructed using the algorithm presented by Raoof and Hassanizadeh (2010). The initial pore-body radii are distributed randomly using a log-normal distribution. The initial throat radii are calculated based on the adjacent pore-body radii using the relation of Joekar-Niasar et al. (2010). The network dimensions and input parameters of the construction are given in Table 4.

The pore bodies on the left are used as inlet pores, and on the right as outlet pores. As for the one-dimensional case 1, the network is initially filled with a saturated solution and an oversaturated solution is injected at the inlet pores. In the two-dimensional case, Dirichlet boundary conditions are applied at the inlet and outlet pores for the primary variables, which fix a constant pressure gradient. At the top and the bottom Neumann no-flow boundary conditions are applied. Details of the initial and boundary conditions are given in Table 5. As for the one-dimensional cases, the time-step size is chosen smaller than the residence time of the fluid in the throat.

The Peclet number for the two-dimensional setup is initially $\mathrm{Pe} = \frac{v_{ij,\mathrm{mean}} l_{ij}}{D_{\mathrm{m}}} = 143.5$. The Damköhler number is initially $\mathrm{Da} = \frac{k A_{\mathrm{react},i} (\Omega - 1)}{Q_{\mathrm{m,mean}} x^{\mathrm{NaCl}}} = 0.0012$. Here $v_{ij,\mathrm{mean}}$ and $Q_{\mathrm{m,mean}}$ are mean velocity and mean molar flux of all throats. As in the one-dimensional case the

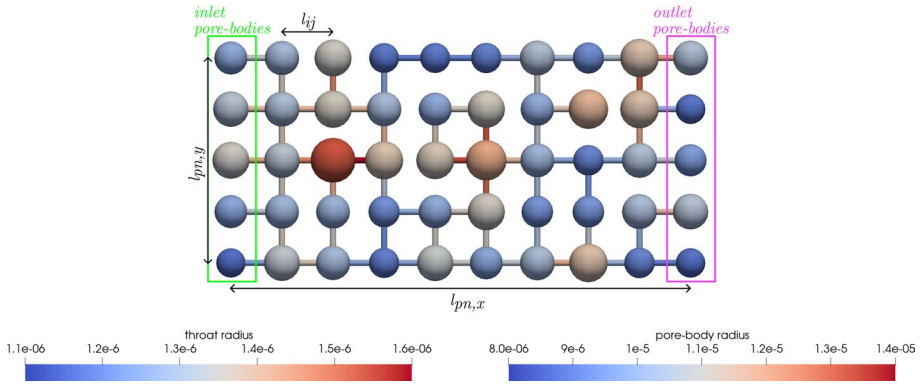

Fig. 5 Two-dimensional setup with 5×10 pore bodies with randomly distributed radii and corresponding varying throat radii. The dimensions can be found in Table 4

Table 4 Dimensions of the two-dimensional pore-network

Pore-network entity	Parameter	Size	Description
Pore bodies	$R_{i,\mathrm{mean}}$	1.0×10^{-5} m	Initial mean pore-body radius
	$\mathrm{std}(R_i)$	1.0×10^{-5} m	Initial standard deviation of the pore-body radius distribution
Pore throats	l_{ij}	3.0×10^{-5} m	Pore-throat length
Pore-network	$l_{\mathrm{pn},x}$	27×10^{-5} m	Length of the entire pore-network system in x-direction
	$l_{\mathrm{pn},y}$	12×10^{-5} m	Length of the entire pore-network system in y-direction

Table 5 Boundary and initial conditions of the two-dimensional pore-network

	Parameter	Size	Description
Boundary conditions	p_{inlet}	1.027×10^5 Pa	Pressure at inlet pore-bodies
	$\phi_{\mathrm{s,inlet}}$	0.0	Inlet precipitated volume fraction
	$x_{\mathrm{inlet}}^{\mathrm{NaCl}}$	0.1	Inlet salt mole fraction
	T_{inlet}	293.15 K	Inlet temperature
	p_{outlet}	1.0×10^5 Pa	Pressure at outlet pore-bodies
	$\phi_{\mathrm{s,outlet}}$	0.0	Outlet precipitated volume fraction
	$x_{\mathrm{outlet}}^{\mathrm{NaCl}}$	0.0996	Outlet salt mole fraction
	T_{outlet}	293.15 K	Outlet temperature
Initial conditions	p_{ini}	$\frac{(p_{\mathrm{inlet}}-p_{\mathrm{outlet}})x}{l_{\mathrm{pn},x}} + p_{\mathrm{inlet}}$	Initial pressure
	$\phi_{\mathrm{s,ini}}$	0.0	Initial precipitated volume fraction
	$x_{\mathrm{ini}}^{\mathrm{NaCl}}$	0.1 for inlet pore bodies 0.0996 for remaining pores	Initial salt mole fraction
	T_{ini}	293.15 K	Initial temperature

advective velocity dominates over the diffusive as well as the reaction velocity. The advective flux, however, is higher and the dimensionless numbers are in a comparable order of magnitude as for the one-dimensional case with higher molar flux $Q_{\mathrm{m,4,high}}$.

4.1.3 Calculation of Upscaled Global Parameters

To evaluate the overall change of a pore-network system due to precipitation, the upscaled permeability K can be calculated using Darcy's law and the continuity equation. The following relation is derived using the total mass flux through the system $Q_{\mathrm{mass,\,pn}}$, the pressure difference $\Delta p = p_{\mathrm{outlet}} - p_{\mathrm{inlet}}$ between inlet and outlet pore body and the cross-sectional area of the system A_{pn}.

$$Q_{\mathrm{mass,\,pn}} = A_{\mathrm{pn}} v = -A_{\mathrm{pn}} K \frac{\rho_{\mathrm{pn}}}{\mu_{\mathrm{pn}}} \Delta p \;\rightarrow\; K = -\frac{Q_{\mathrm{mass,\,pn}}}{A_{\mathrm{pn}}} \frac{\mu_{\mathrm{pn}}}{\rho_{\mathrm{pn}}} \frac{1}{\Delta p}. \tag{55}$$

For A_{pn} the squared diameter of the pore bodies is used in case of the one-dimensional setup. In case of the two-dimensional setup, A_{pn} is calculated by multiplying the initial mean diameter of the pore bodies with the length of the pore-network system in y-direction $l_{\mathrm{pn,y}}$.

The density and viscosity of the fluid change spatially over the domain as different salt concentrations occur. For simplicity, values of ρ_i and μ_i are averaged arithmetically over the total number of pore bodies $N_{\mathrm{pn,body}}$ in the domain weighted by their individual pore-body volume V_i:

$$\rho_{\mathrm{pn}} = \frac{\sum_{i=0}^{N_{\mathrm{pn,body}}} \rho_i \cdot V_i}{\sum_{i=0}^{N_{\mathrm{pn,body}}} V_i}, \tag{56}$$

$$\mu_{\mathrm{pn}} = \frac{\sum_{i=0}^{N_{\mathrm{pn,body}}} \mu_i \cdot V_i}{\sum_{i=0}^{N_{\mathrm{pn,body}}} V_i}. \tag{57}$$

Further, we introduce a global measure to evaluate the distribution of the precipitated salt between the pore throats and pore bodies. The volume fraction of precipitate in throats f_{throat} is defined as the fraction of the sum of the precipitated volume in throats $V_{\mathrm{s},ij}$ over all throats of the pore-network system over the sum of the precipitated volume in all pore throats $V_{\mathrm{s},ij}$ and bodies $V_{\mathrm{s},i}$.

$$f_{\mathrm{throat}} = \frac{\sum_{ij=01}^{\mathrm{N_{pn,throat}}} V_{\mathrm{s},ij}}{\sum_{ij=01}^{\mathrm{N_{pn,throat}}} V_{\mathrm{s},ij} + \sum_{i=0}^{\mathrm{N_{pn,body}}} V_{\mathrm{s},i}}, \tag{58}$$

$$V_{\mathrm{s},ij} = V_{\mathrm{ini},ij} - V_{ij}, \tag{59}$$

$$V_{\mathrm{s},i} = V_{\mathrm{ini},i}\phi_{\mathrm{s},i}. \tag{60}$$

4.2 Comparison of CAPs

In this section the CAPs are compared, which are presented in Sect. 3.1. Circular and rectangular (initially with $B = \frac{1}{3}$) throat cross sections are considered. To calculate the transmissibility, CT1 is used, see Sect. 3.2.1. For CAP4, the pore throat is divided in two throat sections.

4.2.1 One-Dimensional Case 1

For the one-dimensional case 1 a strong difference in the development of the network permeability can be observed between the CAPs, for circular as well as for rectangular throat cross sections, see Fig. 6a and b. For both cross-sectional shapes, the qualitative differences between the CAPs are the same: permeability decreases the most for CAP4, less decrease is observed for CAP3 and even less for CAP1 in case of a circular cross section, while the smallest decrease of permeability is found by CAP2. The initial permeability for the rectangular throat cross section is in general smaller as the rectangular cross section has the same initial area as the circular one, but a larger perimeter. This leads to higher wall friction.

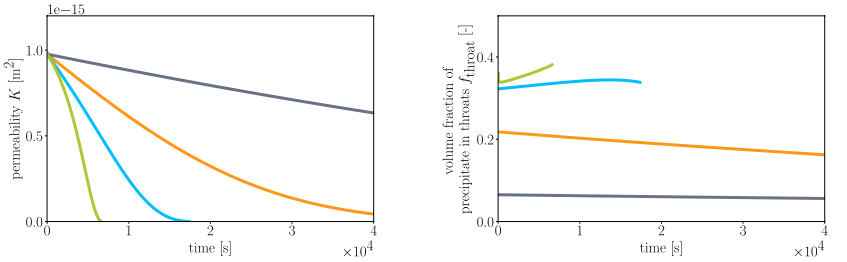

(a) Results for the one-dimensional case 1 for circular throat cross-sections.

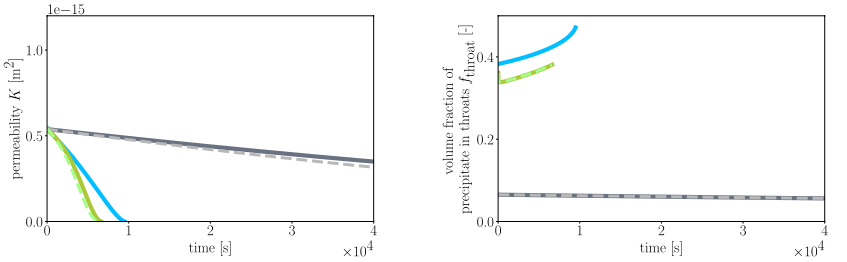

(b) Results for the one-dimensional case 1 for rectangular throat cross-sections.

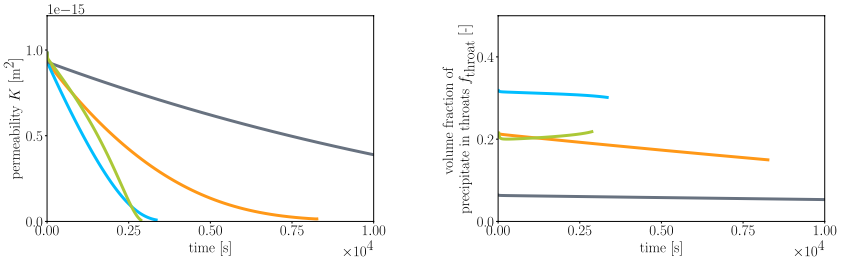

(c) Results for the one-dimensional case 1 for circular throat cross-sections with higher Q.

Fig. 6 Comparison of the different CAPs for the one-dimensional case 1. The plots on the left show the development of the permeability over time and on the right the fraction of precipitation in the throats f_{throat} over time

The difference in permeability development between the CAPs is caused by different percentages of the total precipitated volume being actually in the throats f_{throat}. This ranges from around 7% of the precipitated volume in the throats for CAP2 to 38% for CAP4 for circular throats and up to 47% for CAP3 for rectangular throats.

For the rectangular shape, the permeability is lower using the assumption of constant precipitation thickness than using the assumption of constant rectangle ratio for all CAPs. For the assumption of constant precipitation thickness, the aspect ratio $B = \frac{h}{w}$

of the rectangle decreases. Consequently the ratio of wall length to cross-sectional area gets larger. This leads to a larger decrease in transmissibility of the throat due to higher wall friction than if a constant aspect ratio B is assumed.

In Fig. 7, the development of the precipitated volume fractions in the individual pore bodies and throats for circular throat cross-sections is shown, which describes the precipitated volume in one pore body or throat over the initial volume of the respective body or throat. Most of the salt precipitates in the first pore body and the first pore throats as the oversaturated solution is injected here. Thus, the system shows an inhomogeneous distribution of precipitation. In case of CAP2, the first pore body clogs faster than the first throat, whereas for CAP1, CAP3 and CAP4 the first throat clogs faster than the pore body. Which pore-network element clogs first is related to f_{throat}. In case of CAP3 and CAP4 the simulation aborts due to clogging. For the other two concepts the simulation ends at the end time of the simulation.

For a higher molar flux $Q_{\text{m,4,high}}$ more salt is transported in the system, which leads to faster precipitation and permeability decrease, see Fig. 6c. The qualitative differences in the permeability and f_{throat} are the same as for the lower $Q_{\text{m,4,}}$, except for CAP4. The permeability has not the fastest decrease as for the lower $Q_{\text{m,4,}}$. Also f_{throat} of CAP4 has a lower value of averaged 0.21 compared to 0.36 for the lower $Q_{\text{m,4,}}$. For the other CAPs, however, f_{throat} is nearly the same, independent of Q. The higher flux leads to transport of more salt in the downstream pores and thus to a more homogeneous precipitation distribution throughout the system. For the inhomogeneous precipitation in case of the lower Q the most salt precipitates in the first pore body after the inlet. For CAP4 this is a pseudo pore-body, which leads to high percentages of the precipitate being in the throat. For the other CAPs, most salt precipitates in the first pore body. For CAP4 in case of higher flux, more salt is transported to the regular pore bodies, which leads to a lower f_{throat}. For the other CAPs, this difference does not arise as the amount of precipitate in the throats is not calculated separately from the amount of precipitation in the pore bodies.

4.2.2 One-Dimensional Case 2

Also for the one-dimensional case 2 the permeability development differs between the CAPs, see Fig. 8. Initially the permeability decreases due to the initial oversaturation of the solution until it gets constant as the initially present amount of salt exceeding the solubility limit is precipitated and fluid with equilibrium concentration is injected at the inlet. Except for CAP4, the qualitative differences between the CAPs are the same as for the one-dimensional case 1: CAP2 shows the smallest decrease in permeability, CAP1 has a larger decrease and CAP3 has the largest decrease of permeability. Unlike for the one-dimensional case 1, CAP4 has not the largest permeability decrease, but is between the development of CAP2 and CAP1.

Correspondingly f_{throat} differs for the different CAPs. The higher f_{throat} is, the larger the decrease in permeability is. The value of f_{throat} of each CAP has a comparable size as for the one-dimensional case 1. The exception is CAP4, which has with 9% a lower percentage of precipitate in the throat for the one-dimensional case 2 than for case 1 with 34−38%.

Like the more homogeneous precipitation due to the higher flux $Q_{\text{m,4,high}}$ in case 1, the even more homogeneous distribution in case 2 causes the different behaviour of CAP4. Since the same initial oversaturation is applied in all pore bodies and pseudo pore bodies,

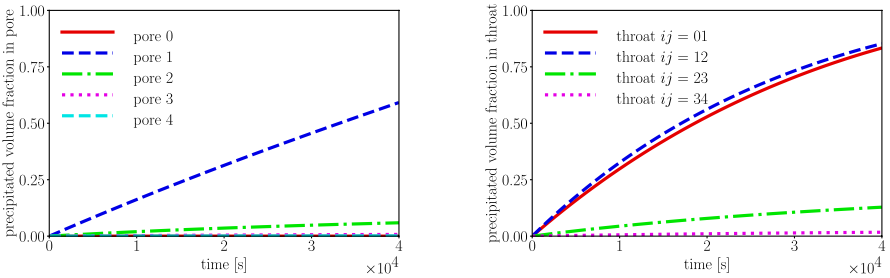

(a) CAP1: concept of relative pore-body volume change from Nogues et al (2013).

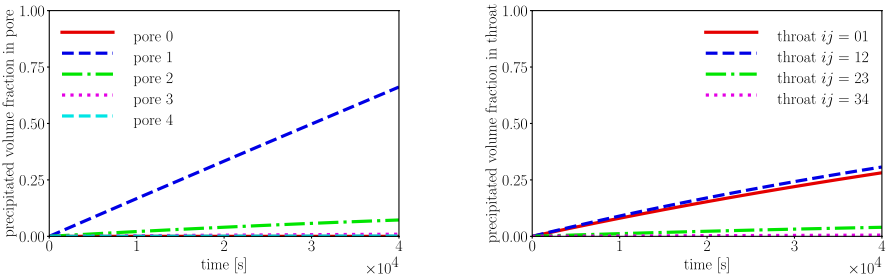

(b) CAP2: concept of average source.

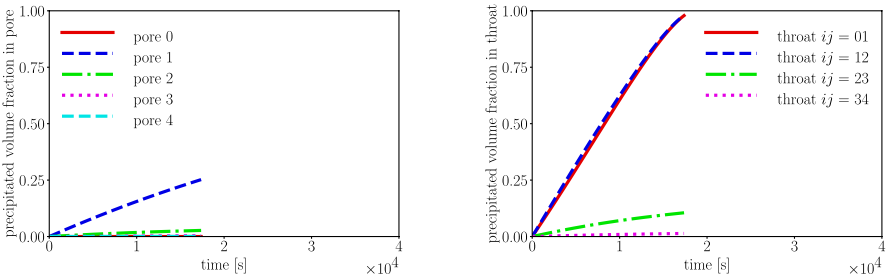

(c) CAP3: concept of linear growth.

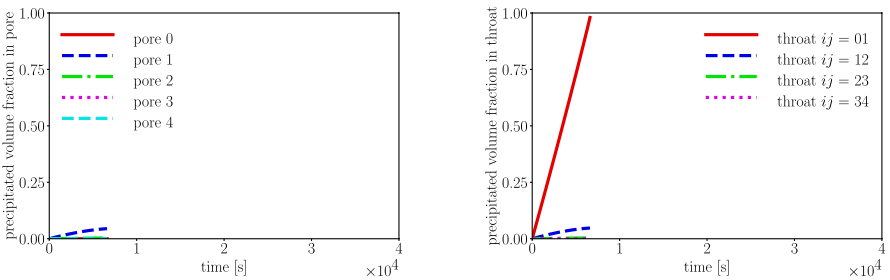

(d) CAP4: concept of a thin tube (2 throat sections).

Fig. 7 Precipitated volume fraction (precipitated volume in body or throat over initial volume of the respective body or throat) in individual pore bodies and throats for the one-dimensional case 1 for circular throat cross sections

but the pore bodies have a larger reactive surface than the throats, most of the salt precipitates in the pore bodies, leading to a low f_{throat}.

In Fig. 9, the homogeneous precipitation behaviour of the case is visible. Nearly the same amount of salt precipitates in every pore body for all CAPs. The amount in pore body 2 is a bit lower due to diffusion of the salt out of the inlet and advective transport of the solution at equilibrium from the inlet. Within each CAP, also the amount of precipitation in the individual throats is nearly the same except for throat 1. This is caused by the fact that in pore body 1, the inlet pore, nothing is precipitating as ϕ_s and x^{NaCl} are fixed by the Dirichlet boundary condition.

4.2.3 Two-dimensional case

To evaluate the two-dimensional calculations, the precipitation distribution in the pore network is considered after 2000 s. For the CAPs, the precipitated volume fraction ϕ_s in the pore bodies and throats is shown in Fig. 10. We first evaluate the precipitation distribution

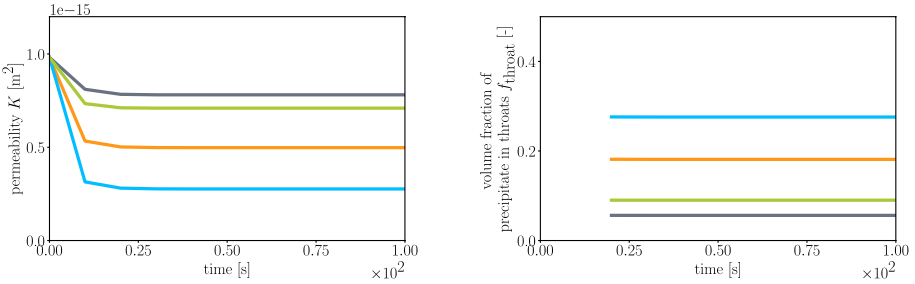

(a) Results for the one-dimensional case 2 for circular throat cross-sections.

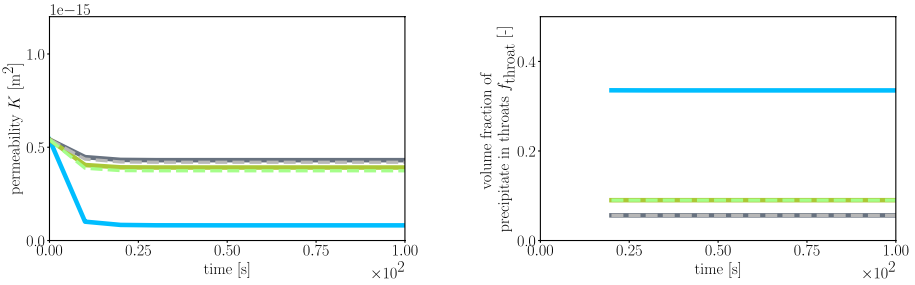

(b) Results for the one-dimensional case 2 for rectangular throat cross-sections.

Fig. 8 Comparison of the different CAPs for the one-dimensional case 2. The plots on the left show the development of the permeability and on the right the fraction of precipitation in the throats f_{throat} over time (for the latter the value for $t = 0$ is missing because the total precipitated volume, which is divided by to obtain the volume fraction, is zero here)

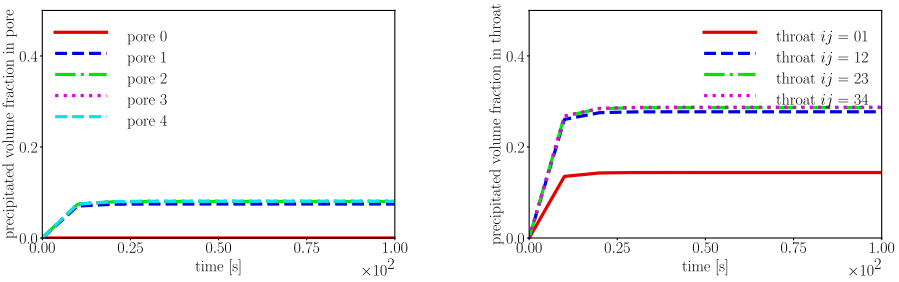

(a) CAP1: concept of relative pore-body volume change from Nogues et al (2013).

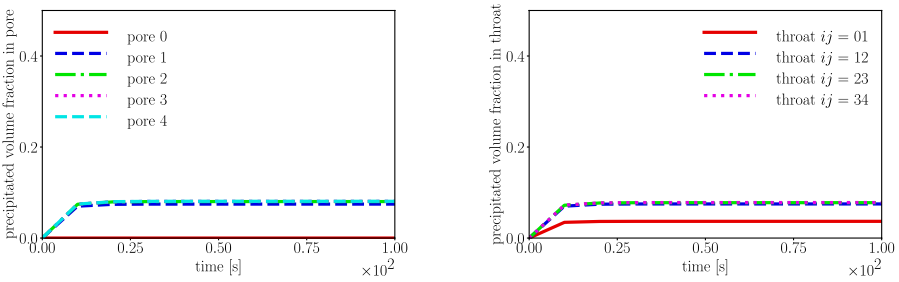

(b) CAP2: concept of average source.

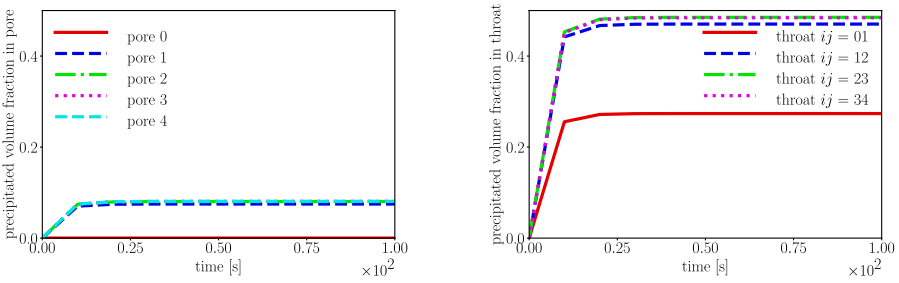

(c) CAP3: concept of linear growth.

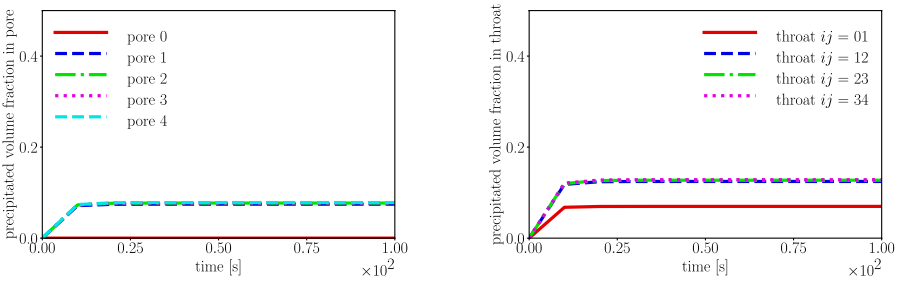

(d) CAP4: concept of a thin tube (2 throat sections).

Fig. 9 Precipitated volume fraction (precipitated volume in body or throat over initial volume of the respective body or throat) in individual pore bodies and throats for the one-dimensional case 2 for circular throat cross sections

Fig. 10 Results of the two-dimensional pore-network at $t = 2000$ s. On the left is the precipitated volume fraction of the pore bodies and throats for the different CAPs. On the right the difference of the individual CAP to CAP3 is shown. Here positive values (red) indicate larger values than CAP3 and negative values (blue) indicate smaller values

for CAP3 (Fig. 10a). Afterwards it is used as reference to calculate the difference in ϕ_s to CAP3 for the remaining CAPs to compare the distributions of precipitation, see Fig. 10b–d (right side).

For CAP3 most of the salt precipitates in the first column of pore bodies after the inlet pores, as here the solution has the highest oversaturation. The amount of precipitate gets less towards the outlet pores on the right side. More precipitation in the pore bodies and throats are observed towards the right side if the pore-bodies are connected in x-direction along the direction of the pressure gradient. In this case the advective flux transports the dissolved salt towards the right. This is for example the case in the bottom row of the network. In dead ends less precipitation is observed. Less salt is transported in these pore bodies due to smaller pressure gradients. Here, the transport is diffusion dominated.

The other CAPs generate in general a similar distribution of the precipitate in the whole pore network. The main difference is how much salt is located in the pore throats compared to the pore bodies. In general the differences are larger in pores and throats with large values of ϕ_s and less in, for example, dead ends. CAP1 has more precipitation in the pore bodies and less precipitation in the pore throats, in comparison with CAP3. The maximal difference in ϕ_s is 0.016 for pore bodies and 0.24 for throats. CAP2 has also more precipitation in the pore bodies and less in the pore throats compared to CAP3. For this approach, the deviation is even larger. The maximal difference in ϕ_s is 0.042 for pore bodies and 0.57 for pore throats. CAP4 has relatively small differences compared to CAP3. Here, some pore bodies show more and some less precipitation. The maximal difference of ϕ_s is 0.016 for the pore bodies. If the results are compared at the end of each simulation (when either a pore body or throat is fully clogged) CAP4 shows less precipitation in all pore bodies. The values of both throat sections are equal in case of two sections, as the calculation is based on one pseudo pore body and the amount of precipitation is distributed equally between the sections. This one value of precipitated volume fraction is used for the comparison with CAP3. CAP4 shows a higher precipitated volume fraction in the first throats after the inlet with a maximal difference of 0.41 and less in the remaining pore-network system with a maximal difference of 0.24.

The same distribution of the precipitate between pore bodies and throats of the different CAPs can be seen in the global values for the entire network, see Fig. 11. The largest f_{throat} is found for CAP3, the second largest for CAP1, the third largest for CAP4 and the lowest ratio has CAP2. This corresponds to the permeability development, where the largest ratio indicates the highest amount of precipitation in the throats and consequently the smallest permeability. The qualitative distribution of permeability development between the CAPs is similar compared to the one-dimensional simulations of case 1 with higher Q, as the Peclet numbers and Damköhler numbers of these cases are in the same order of magnitude.

4.3 Influence of the Number of Throat Sections for CAP4

The influence of the number of throat sections for CAP4 is investigated for both one-dimensional cases using circular cross-sectional shapes. The results for two throat sections,

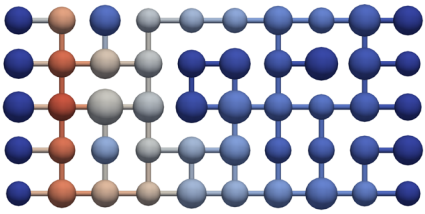

(a) Precipitated volume fraction for CAP3.

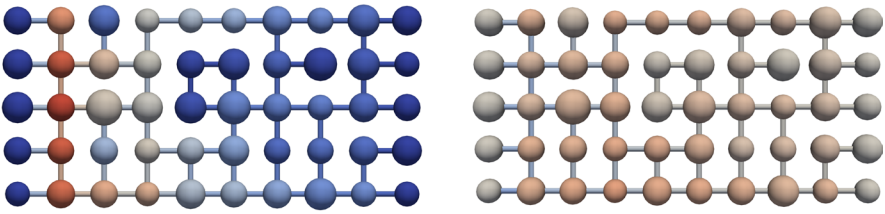

(b) Precipitated volume fraction for CAP1 (left) and difference to CAP3 (right).

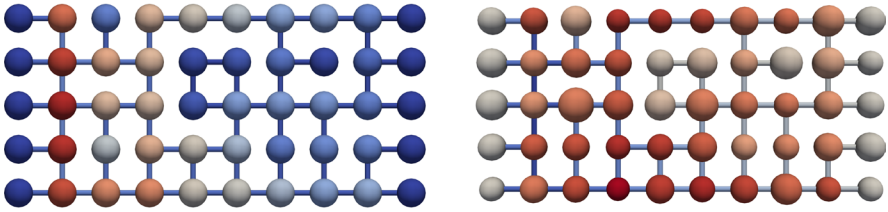

(c) Precipitated volume fraction for CAP2 (left) and difference to CAP3 (right).

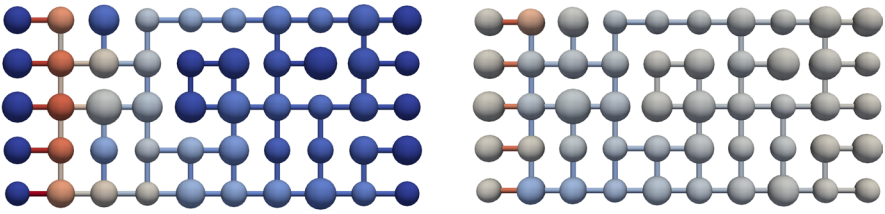

(d) Precipitated volume fraction for CAP4 (left) and difference to CAP3 (right).

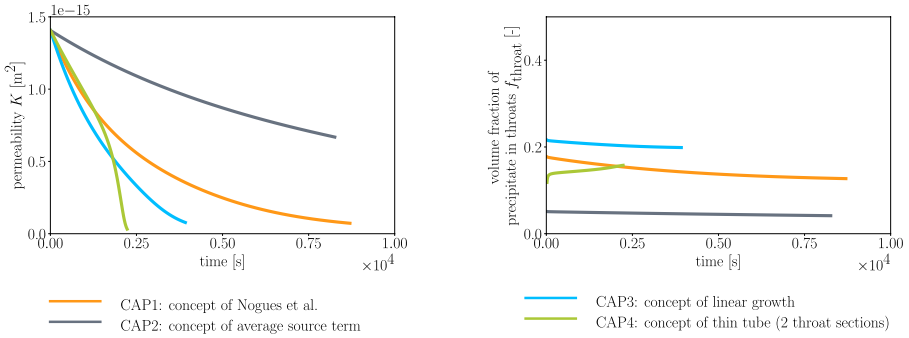

Fig. 11 Comparison of the different CAPs for the two-dimensional pore network. The plots on the left show the development of the permeability over time and on the right the fraction of precipitation in the throats f_{throat} over time

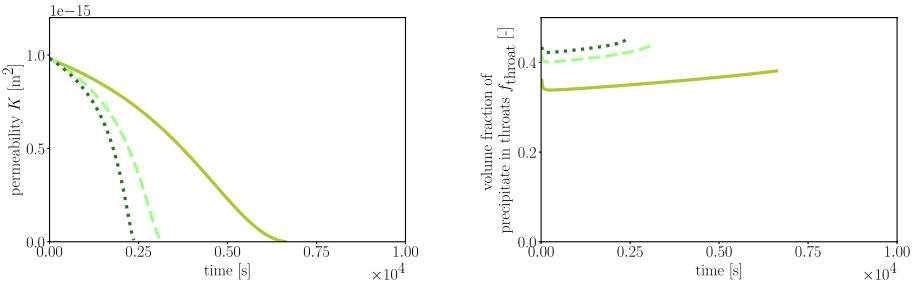

(a) Results for CAP4 for the one-dimensional case 1.

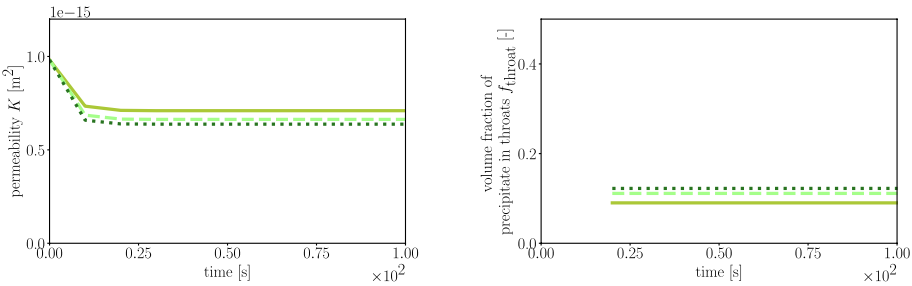

(b) Results for CAP4 for the one-dimensional case 2.

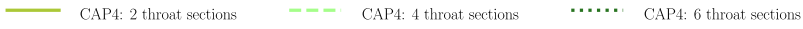

Fig. 12 Comparison of different number of throat sections for CAP4. The plots on the left show the development of the permeability over time and on the right the fraction of precipitation in the throats f_{throat} over time

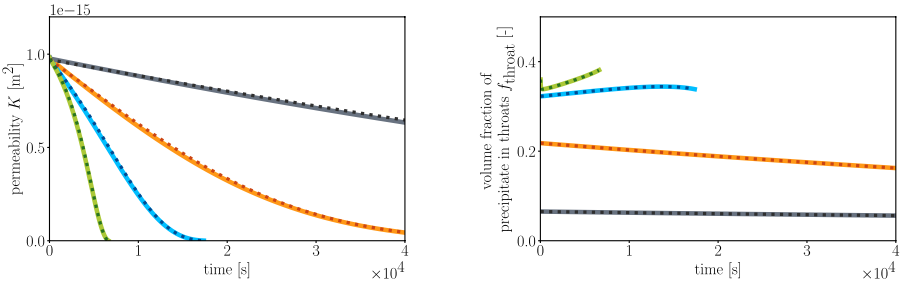

(a) Results for the one-dimensional case 1 for circular throat cross-sections.

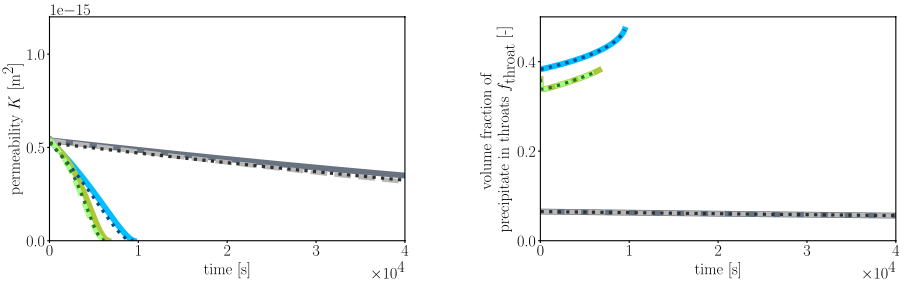

(b) Results for the one-dimensional case 1 for rectangular throat cross-sections.

Fig. 13 Comparison of the two CTs for the one-dimensional case 1. The plots on the left show the development of the permeability and on the right the fraction of precipitation in the throats f_{throat} over time

already presented in the previous section, is compared to the division in 4 and 6 throat sections per pore throat.

With the increase of the number of throat sections, a faster decrease in permeability can be observed, see Fig. 12. The one-dimensional case 1 with a core area of precipitation at the inlet, emphasizes the differences between the different numbers of used throat sections. Based on the injection of oversaturated solution, most of the salt precipitates at the inlet of the pore-network system. The smaller the length of the first throat sections is, the larger is the precipitated volume fraction. This is due to the smaller throat section volume by a comparable amount of precipitate. For the one-dimensional system, the narrowing of one throat or throat section controls the permeability of the whole pore-network system. This results in the faster decrease in permeability of the system. Further, this leads to the faster clogging of the throat section. For the one-dimensional case 2, less differences between the different number of throat sections are observed as a comparable amount of salt precipitates throughout the whole system.

With the number of throat sections f_{throat} increases. The difference of the values is here much larger for the one-dimensional case 1 than for case 2.

Table 6 Comparison of the concepts for the amount of precipitation in the pore throat

CAPs	Body throat relation	$\Delta r_{ij}^{\Delta t}$ for circular cross section
CAP1	$\Delta r_{ij}^{\Delta t} \sim \Delta V_{\text{body}}^{\Delta t}$	$r_{ij}^{t-1}\left(\frac{\Delta V_i^{\Delta t}}{V_i^{t-1}}+\frac{\Delta V_j^{\Delta t}}{V_j^{t-1}}\right)$
CAP2	$\Delta V_{ij}^{\Delta t} \sim \Delta V_{\text{body}}^{\Delta t}$	$\frac{1}{2}\frac{(r_{ij}^{t-1})^2}{r_{ij}^t+r_{ij}^{t-1}}\left(\frac{\Delta V_i^{\Delta t}}{V_i^{t-1}}+\frac{\Delta V_j^{\Delta t}}{V_j^{t-1}}\right)$
CAP3	$\Delta r_i^{\Delta t} = \Delta R_i^{\Delta t}$	$\left(\frac{3(r_i^t)^3(r_j^t)^3}{(r_i^t)^2+r_i^t r_j^t+(r_j^t)^2}\right)^{\frac{1}{4}} - \left(\frac{3(r_i^{t-1})^3(r_j^{t-1})^3}{(r_i^{t-1})^2+r_i^{t-1}r_j^{t-1}+(r_j^{t-1})^2}\right)^{\frac{1}{4}}$
		$r_i^t = r_i^{t-1} + \left(\frac{3}{4\pi}\right)^{\frac{1}{3}}\left(\left(V_i^{t-1}+\Delta V_i^{\Delta t}\right)^{\frac{1}{3}} - \left(V_i^{t-1}\right)^{\frac{1}{3}}\right)$
CAP4	There exists no direct relation between body and throat	

4.4 Comparison of CTs

The two CTs introduced in Sect. 3.2, are analysed and compared in this section, see Fig. 13. We combine CAP3 with CT2 here. It is noted, that CAP3 assumes a linear salt-layer thickness along the throat whereas CT2 assumes a constant thickness. In this context, CAP3 is only used to calculate the new throat volume based on the effective averaged throat dimensions (Eqs. (28) and (29)) and CT2 calculates the new transmissibility.

For circular cross sections, the two CTs give similar results. For rectangular cross sections, tiny differences are visible. Here, the permeability from CT2 is between the results using CT1. With the assumption of a constant B, the permeability is larger, while with the assumption of a constant δ, the permeability is lower than the results from CT2. Between the different CTs is no difference in f_{throat} as the amount of precipitate in the throat is determined by the CAP and not directly influenced by the CT. Due to the small differences in the permeability between the CTs the influence of different transport of salt through the network based on the different transmissibilities has a negligible influence on the precipitation distribution.

The results show the similarity of the approaches for simple cross-sectional shapes like circles and rectangles. Here, the different assumptions for the shape of the precipitate in the throat of the different CTs do not have a great influence on the transmissibility of the throats.

5 Discussion

5.1 Concepts for Amount of Precipitation

The CAPs in the pore throats have a large influence on the permeability of the pore-network system. To compare the CAPs, the relation between the change of pore-throat dimensions and the change in the pore-body dimensions are further analysed. This shows how the change in pore-body volume influences the throat radii in the different CAPs. Therefore the relations of Sect. 3.1 are reformulated. Also the influence of the CAPs on f_{throat} is discussed. The comparison of the CAPs is summarized in Table 6.

For CAP1, Eq. (12) is reformulated to describe the change in throat radius:

$$\Delta r_{ij}^{\Delta t} = r_{ij}^{t-1}\left(\frac{\Delta V_i^{\Delta t}}{V_i^{t-1}} + \frac{\Delta V_j^{\Delta t}}{V_j^{t-1}}\right), \tag{61}$$

$$\Delta r_{ij}^{\Delta t} \sim \Delta V_{\text{body}}^{\Delta t}, \tag{62}$$

where $\Delta r_{ij}^{\Delta t} = r_{ij}^{t} - r_{ij}^{t-1}$ and $\Delta V_i^{\Delta t} = V_i^t - V_i^{t-1}$ is the change in throat radius and volume in one time step. This shows that the change in throat radius is proportional to the change in pore-body volumes for CAP1.

To analyse the relationship between the change in pore-throat and pore-body dimensions of CAP2, the meaning of the source term in the pore body is considered:

$$\Delta V_i^t = V_i^t - V_i^{t-1} = \frac{s_i^t\,\Delta t}{\rho_{\text{m,s}}^{t-1}}, \tag{63}$$

$$\rightarrow s_i^t = \left(V_i^t - V_i^{t-1}\right)\frac{\rho_{\text{m,s}}^{t-1}}{\Delta t}. \tag{64}$$

If Eq. (64) is inserted in Eq. (15), we get the following relationship:

$$\frac{\Delta V_{ij}^{\Delta t}}{V_{ij}^{t-1}} = \frac{1}{2}\left(\frac{\Delta V_i^{\Delta t}}{V_i^{t-1}} + \frac{\Delta V_j^{\Delta t}}{V_j^{t-1}}\right), \tag{65}$$

$$\Delta V_{ij}^{\Delta t} \sim \Delta V_{\text{body}}^{\Delta t}. \tag{66}$$

This shows that CAP2 relates the throat volume change to the pore-body volume change. For the comparison with CAP1, Eq. (65) can be rearranged in the form of Eq. (61), e.g. for circular throat cross sections:

$$\Delta r_{ij}^{\Delta t} = \frac{1}{2}\frac{\left(r_{ij}^{t-1}\right)^2}{r_{ij}^{t} + r_{ij}^{t-1}}\left(\frac{\Delta V_i^{\Delta t}}{V_i^{t-1}} + \frac{\Delta V_j^{\Delta t}}{V_j^{t-1}}\right). \tag{67}$$

For circular cross sections, the radius change differs with a factor $f = \frac{1}{2}\frac{r_{ij}^{t-1}}{r_{ij}^{t}+r_{ij}^{t-1}}$ from CAP1. This factor is $f < 1$, thus the relative radius change is smaller in each time step, which leads to higher transmissibilities as shown in the result Sect. 4.

For CAP3, Eq. (18) can be reformulated so it is visible that this concept relates the change in pore-body radius to the change in throat radius:

$$\Delta r_i^{\Delta t} = \Delta R_i^{\Delta t}. \tag{68}$$

The average radius change for the whole throat can be expressed using the effective radius (Eq. (28)) and the change in throat end radius for spherical pore bodies (Eqs. (17) and (18)):

$$\Delta r_{ij}^{\Delta t} = \left(\frac{3(r_i^t)^3 (r_j^t)^3}{(r_i^t)^2 + r_i^t r_j^t + (r_j^t)^2} \right)^{1/4} - \left(\frac{3(r_i^{t-1})^3 (r_j^{t-1})^3}{(r_i^{t-1})^2 + r_i^{t-1} r_j^{t-1} + (r_j^{t-1})^2} \right)^{1/4}, \tag{69}$$

$$r_i^t = r_i^{t-1} + \left(\frac{3}{4\pi} \right)^{1/3} \left(\left(V_i^{t-1} + \Delta V_i^{\Delta t} \right)^{1/3} - \left(V_i^{t-1} \right)^{1/3} \right). \tag{70}$$

For CAP4, the change in throat radius is based on the source term in the throat section. It is not directly depending on the precipitation in the pore body, but connected through the fluid flow. In contrast to the other concepts, it also includes upwinding, therefore only the properties of the upstream body influence the throat.

The CAPs can be further analysed, by comparing f_{throat} for the different considered cases. For CAP1 and CAP2, f_{throat} is relatively constant for all cases and independent of the cross-sectional shape. For CAP2 this can be analysed easily for the assumption that in all pore bodies the same amount is precipitating, like in the one-dimensional case 2. For this, Eq. (65) can be simplified and reformulated:

$$\frac{\Delta V_{ij}^{\Delta t}}{V_{ij}^{t-1}} = \frac{\Delta V_i^{\Delta t}}{V_i^{t-1}} \rightarrow f_{\text{throat}} = \frac{\Delta V_{ij}^{\Delta t}}{\Delta V_i^{\Delta t}} = \frac{V_{ij}^{t-1}}{V_i^{t-1}} = \frac{V_{ij,\text{ini}}}{V_{i,\text{ini}}}. \tag{71}$$

This shows that f_{throat} is only dependent on the initial geometry of the pore network for CAP2. For the one-dimensional setup $f_{\text{throat}} = 0.075$, which corresponds with the results of the simulations. For CAP3, f_{throat} varies between the setups and depends on the cross-sectional shape of the throat. The biggest variation of f_{throat} can be observed for CAP4. As already discussed in the result section, for this concept f_{throat} is strongly influenced by the distribution of the precipitation. For a inhomogeneous precipitation, as in the one-dimensional case 1, f_{throat} is high as most of the salt is precipitating in the first throat. Whereas for the homogeneous precipitation f_{throat} is lower as here the amount of precipitation depends mainly on the reactive surface area A_{react}, which is higher in the pore bodies. In contrast to the other CAPs, the amount of precipitation in the throat in CAP4 is not directly dependent on the amount of precipitation in the pore body. This enables the higher variation in f_{throat}.

5.2 Concepts of Transmissibility Calculation

The results of the two CTs do not differ much for the considered throat cross-sectional shapes. The difference between the CTs is the assumption on the distribution of the precipitation within the throat cross section. This leads to tiny differences in the transmissibility for cross-sectional shapes where the precipitation in an equally thick layer alters the shape, for e.g. rectangles.

From a physical point of view, the assumption of an equally thick precipitation layer seems more plausible than the constant cross-sectional shape as this results from a homogeneous precipitation at the throat wall. To keep the cross-sectional shape constant, more salt has to precipitate at some edges than at others, which has no physical reason.

6 Final Remarks

We have developed a pore-network model to simulate salt precipitation in porous media for saturated flow. The throats in a pore-network determine the resistance of the pore-network system and have a great influence on the overall flow behaviour. Thus, different concepts to determine the amount of precipitate in the throats (CAPs) and to calculate the throat transmissibility (CTs) were introduced for two different cross-sectional shapes: circular and rectangular. For a saturated pore-network system, the concepts were compared for two different one-dimensional cases for circular and rectangular throat cross-sections and one two-dimensional case for circular throat cross-sections.

Four concepts to determine the amount of precipitate in the throats (CAPs) have been introduced: the concept of relative pore-body volume change from Nogues et al. (2013) (CAP1), the concept of average precipitation source (CAP2), the concept of linear growth (CAP3) and the concept of a thin tube (CAP4).

CAP1 applies the added relative pore-body volume changes to the throat radius. The concept assumes a correlation between pore-throat radius and the volume of the adjacent pore bodies, which is based on experimental investigations of existing sand-stone pore structures. The remaining concepts use different assumptions about the physical process of precipitation. CAP2 averages the source terms per pore-body volume of the adjacent pore bodies to get the average number of moles which precipitate per volume and time and applies this to the throat volume. This concepts assumes that the same amount of moles precipitates per volume in the bodies and the throats. Here the change in pore-throat volume correlates with the change in pore-body volume. CAP3, however, assumes the same precipitation thickness in the throat ends as in the adjacent pore bodies. The same amount of precipitation per pore wall is assumed for the body and the adjacent throat end. Here the change in pore-throat radius corresponds with the change in pore-body radius. CAP2 and CAP3 differ in the assumption whether the precipitation is dependent on the volume of the pore space and the total amount of dissolved salt in the space or on the reactive area at the pore walls. For CAP4 the precipitation reaction is calculated in the throat by solving the mole balances. The precipitation reaction in the source term of the mole balance depends on the reactive surface. CAP4 differs mostly from the other CAPs by the variable distribution of the salt along the throat and that the precipitated amount of salt in the throats is accounted for in the balance equations.

The CAPs are found to have a great influence on the development of the permeability of the whole pore-network system. They differ mainly in the percentage of the total precipitated volume in the system that is located in the throats f_{throat}. This percentage ranges from 5 to 47% for the different concepts. For the one-dimensional case 1, in which the injection of an oversaturated solution causes an inhomogeneous precipitation pattern in the pore network, f_{throat} increases from CAP2 over CAP1 and CAP3 to CAP4. The permeability decreases accordingly with the increase of f_{throat}. For the one-dimensional case 2, in which the initially present oversaturated solution causes a homogeneous pattern of precipitation in the pore-network, the qualitative differences are the same except for CAP4, which has the second least permeability decrease after CAP2. For CAP4, f_{throat} is strongly dependent on the precipitation distribution, whereas for CAP1 and CAP2 f_{throat} is relatively constant for all cases. For CAP3, f_{throat} depends on the cross-sectional shape. In the two-dimensional case, randomly distributed pore-body and throat radii are used and an oversaturated solution is injected. The qualitative differences in permeability distribution are similar to the one-dimensional case 1. Further,

a detailed analysis of CAP4 showed that the permeability decreases more when more throat sections are used for the one-dimensional case 1.

In addition, two different concepts to calculate the throat transmissibility (CTs) for saturated conditions were used: the concept of Bruus (2011) (CT1) and a phase-field model (CT2). No strong difference of the permeability development of the pore network could be found between the two CTs. In case of circular cross sections, the different assumptions for the distribution of the precipitate in the cross section of the CTs lead to similar precipitation shapes, which leads to similar permeability developments. For rectangular cross sections, slight differences in the precipitate distribution arise, which cause tiny differences in the permeability development. However, the results show a minor influence of the shape of the precipitate on the throat transmissibility.

The decision for which of the concepts to apply depends on different aspects. Considering evaporation-driven precipitation, the salt accumulates at the evaporation front and is not equally distributed in the domain (Jambhekar et al. 2016; Shokri 2014). CAP4 is able to capture inhomogeneous precipitation within the pore-network system more exact as the division of the throat enables non-constant precipitation distribution along the throat. However, the precision of this concept depends on the number of throat sections. CAP3 considers a linear distribution of the precipitate along the throat, while using the same number of unknowns as the other two concepts (CAP1 and CAP2) that have a constant precipitate distribution along the throats. Further aspects for the decision of which concept to use are the complexity of the implementation and the duration of the simulations. Here, CAP1, CAP2 and CAP3 are simple to implement and have low computational costs compared to CAP4, which has a higher number of unknowns.

Consequently, if the assumption of a constant precipitate distribution along the throat is reasonable, for example for homogeneous precipitation or short pore throats, CAP1, CAP2 or CAP3 are sufficient. If a variable distribution of the precipitate along the throat has to be accounted for, for example for inhomogeneous precipitation or long pore throats, CAP4 or CAP3 are reasonable as they consider a variable distribution of the precipitate along the throat.

Concerning the CTs, the difference lies mainly in how general the concept should be in terms of the cross-sectional shape of the pore throat. The existing relations from CT1 are easy to apply for a selected number of cross-sectional shapes, especially when the shape remains. CT2, however, is a more general tool to calculate the transmissibility and can be applied to arbitrary shapes. By coupling the pore-network and phase-field model, arbitrary throat cross-sectional shapes can be modelled. However, the coupled model is computational expensive. Consequently, for large networks and commonly used shapes, the development of the approximated relation is useful, which is a one-time expense and for which the usage has a comparable computationally cost as CT1. The phase-field model is an effective tool to develop new relations for the one-phase transmissibility of pore-throats. For simple shapes this effort is not necessary and the relations from CT1 can be used.

The investigation in this paper is not able to identify the most physical correct approach. Therefore, a comparison with experiments is necessary. Micro-model experiments using a simple setup as in this paper would be ideal for this purpose. Further, the presented model has to be extended to two-phase flow to be able to represent evaporation-driven salt precipitation in porous media on the pore scale. The presented throat concepts have to be extended to represent the case of air invading pore throats with corner flow of saline solution. The CAPs therefore have, to consider the saturation of the throat as salt is only present in the saline phase. To calculate the phase transmissibilities, the CTs have to take into account complex shapes of the throat cross-section occupied by the phases. Therefore,

the extension of the phase-field model to two-phase flow could be helpful to generate new relations.

Appendix A Details About the Implementation of the Concepts

A flow chart of the implementation of the different concepts CAPs and CTs is presented in Fig. 14. The system of equations contains the mole balance equations and closure relationships presented in Sect. 2.1. This system of equations determines the primary variables. Based on the primary variables secondary variables like the actual pore volume V_i^t or radius R_i^t can be calculated. Depending on the CAP different relations are used to determine the actual volume of the pore throat V_{ij}^t. The details of the different concepts are explained in the individual sections. The new throat volume is then used in one of the CTs to calculate the actual throat radius r_{ij}^t or width w_{ij}^t and transmissibility g_{ij}^t. All these relations are included implicit in the system of equations which is solved in every time step. For CAP1, CAP3 and CAP4 the change in throat volume and transmissibility are coupled implicit with the transport described by the mole balance equations. For CAP2, however, an explicit coupling is used where the throat volume of the previous time step is used in the CTs to calculate the transmissibility. After the system has been solved, for CAP1 the parameters such as V_i^t and r_{ij}^t are saved and for CAP2 the actual throat volume V_i^t is calculated for use in the next time step. Finally, in the post-processing, global parameters, described in Sect. 4.1.3, are calculated to evaluate the system.

Appendix B Derivation of Eq. (24)

First the new throat cross-sectional area at the individual pore-throat ends A_i^t is calculated using the assumption of an equal thick precipitation layer $\delta = \text{const}$. For CAP3, the precipitation-layer thickness at the individual pore-throat ends is equal to the precipitation layer thickness in the pore bodies. Here $\Delta R_i^{\Delta t}$ is the change in pore-body radius, which corresponds to the change in the precipitation-layer thickness and is negative in case of precipitation:

$$A_i^t = \left(h_i^{t-1} + 2\Delta R_i\right)\left(w_i^{t-1} + 2\Delta R_i\right). \tag{B.1}$$

The height and width of the rectangle are then determined using the assumption of constant aspect ratio B, which allows us to eliminate the new width w_i^t:

$$B = \frac{w_i^{t-1}}{h_i^{t-1}} = \frac{w_i^t}{h_i^t}. \tag{B.2}$$

$$A_i^t = w_i^t h_i^t = \frac{w_i^{t-1}}{h_i^{t-1}}\left(h_i^t\right)^2. \tag{B.3}$$

Equations (B.1) and (B.3) are set equal and the resulting equation is solver for h_i^t:

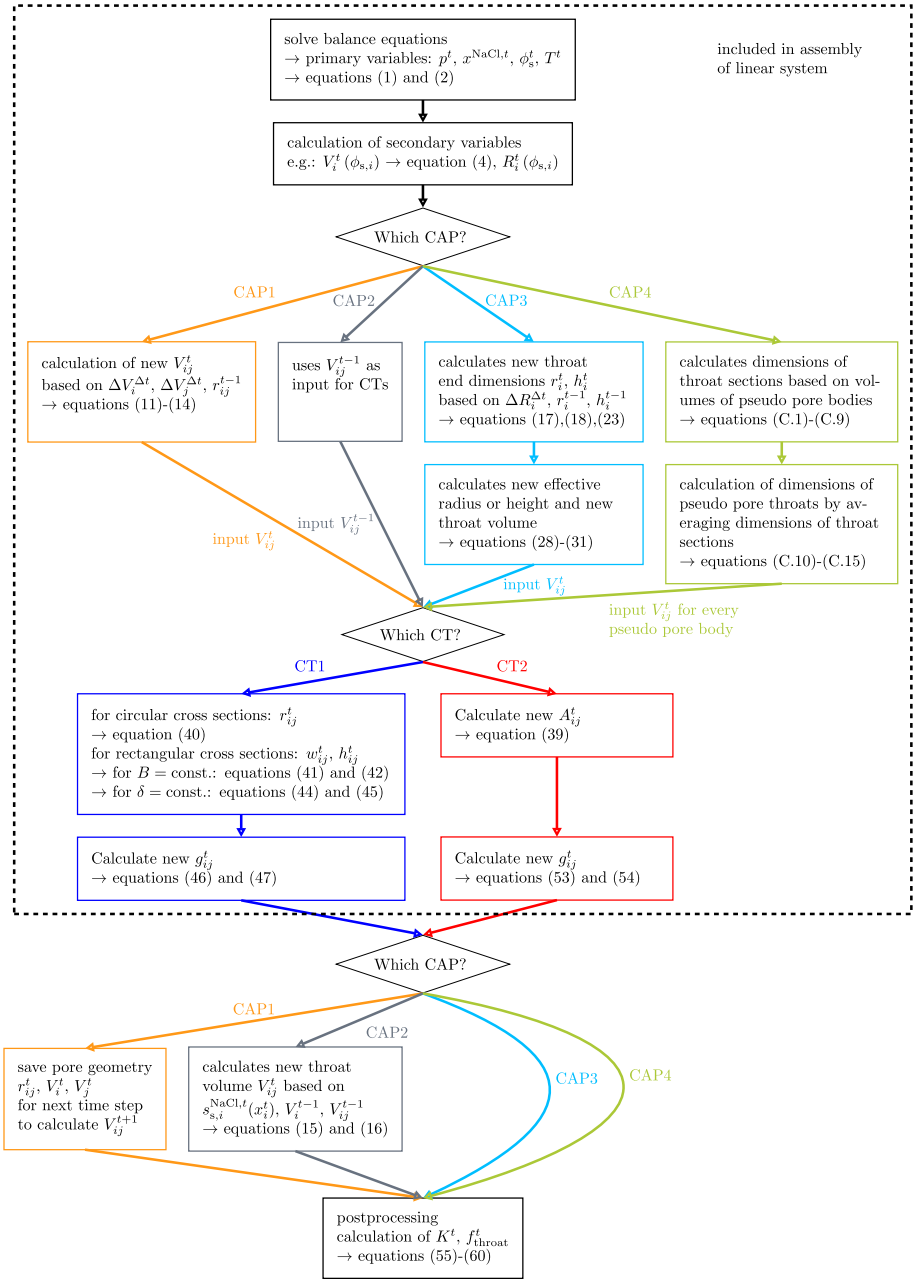

Fig. 14 Flow chart of the implementation of the different concepts presented in this paper

$$\frac{w_i^{t-1}}{h_i^{t-1}}\left(h_i^t\right)^2 = \left(w_i^{t-1} + 2\Delta R_i\right)\left(h_i^{t-1} + 2\Delta R_i\right), \tag{B.4}$$

$$\implies h_i^t = \sqrt{\frac{h_i^{t-1}}{w_i^{t-1}}\left(h_i^{t-1} + 2\Delta R_i^{\Delta t}\right)\left(w_i^{t-1} + 2\Delta R_i^{\Delta t}\right)} \tag{B.5}$$

$$= \sqrt{h_i^{t-1} + 2\Delta R_i^{\Delta t}}\sqrt{h_i^{t-1} + 2B\Delta R_i^{\Delta t}}. \tag{B.6}$$

Appendix C Implementation Details of CAP4

This appendix explains the implementation of the concept of a thin tube (CAP4) in the pore-network model in detail. Figure 15 shows the idea of discretization. CAP4 divides the pore throat in throat sections n. For each of the sections, the mole balance is solved as described in Sect. 3.1.4. For the implementation, each throat section n is represented through one pseudo pore body at position z. The pseudo pore body contains the volume of one throat-section $V_{ij,z} = V_{ij,n}$. The pseudo pore bodies are equally spaced throughout the pore throat. For a pore throat with initially constant dimensions along the throat, the outer pseudo pore bodies, which are adjacent to regular pore bodies, have initially one and a half times of the volume of the inner pore bodies, which are only connected to other pseudo pore bodies. This corresponds to one and a half time longer outer throat sections connected to the regular pore-bodies. If only one pseudo pore body is used per throat it contains the whole volume of the throat as the whole throat is one throat section.

From the balance equations (36) and (37), the volume of the pseudo pore bodies is calculated for every time step. The volume of each pseudo pore body $V_{ij,z}$ is transferred to the volume of the throat section $V_{ij,n} = V_{ij,z}$ and the cross-sectional area of the pore-throat section is calculated. Here the different volumes of the throat sections are considered:

$$\text{for inner pseudo pore bodies} : A_{ij,n}^t = \frac{V_{ij,n}^t}{\Delta l_{ij}}, \tag{C.1}$$

$$\text{for outer pseudo pore bodies} : A_{ij,n}^t = \frac{2V_{ij,n}^t}{3\Delta l_{ij}}, \tag{C.2}$$

$$\text{for use of just one pseudo pore body} : A_{ij,n}^t = \frac{V_{ij,n}^t}{2\Delta l_{ij}}. \tag{C.3}$$

The dimensions of every throat section are calculated in the following for circular and rectangular throat cross sections:

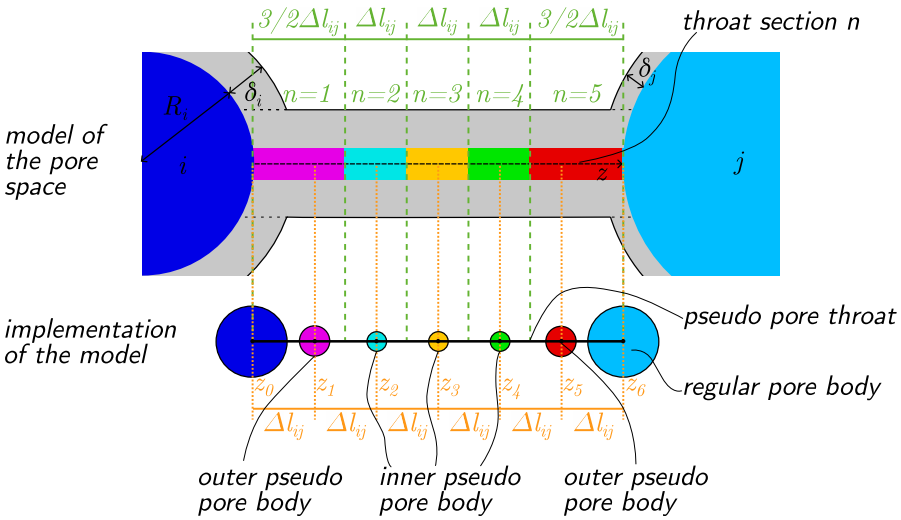

Fig. 15 Implementation of CAP4 in the pore-network model

$$\text{circular}: r_{ij,n} = \sqrt{\frac{A^t_{ij,n}}{\pi}}, \tag{C.4}$$

rectangular $B = \text{const.}$:

$$w^t_{ij,n} = \sqrt{\frac{A^t_{ij,n}}{B}}, \tag{C.5}$$

$$h^t_{ij,n} = B w^t_{ij,n}. \tag{C.6}$$

rectangular $\Delta\delta_{ij} = \text{const.}$:

$$\text{solve } \Delta l_{ij}\left(w^t_{ij,n}\right)^2 + \left(h_{\text{ini}} - w_{\text{ini}}\right)\Delta l_{ij} w^t_{ij,n} - A^t_{ij,n}\Delta l_{ij} = 0, \tag{C.7}$$

$$w^t_{ij,n} = \frac{\left(h_{\text{ini}} - w_{\text{ini}}\right)\Delta l_{ij} + \sqrt{\left(\left(h_{\text{ini}} - w_{\text{ini}}\right)\Delta l_{ij}\right)^2 + 4A^t_{ij,n}\Delta l^2_{ij}}}{2\Delta l_{ij}}, \tag{C.8}$$

$$h^t_{ij,n} = \frac{A^t_{ij,n}}{w^t_{ij,n}}. \tag{C.9}$$

The dimensions of the pseudo pore throats $z, z+1$ between pseudo pore body z and $z+1$ are then calculated with harmonic averaging for the inner pseudo pore throats:

$$r_{ij,z,z+1} = \frac{2r_{ij,n}r_{ij,n+1}}{r_{ij,n} + r_{ij,n+1}}, \tag{C.10}$$

$$w_{ij,z,z+1} = \frac{2w_{ij,n}w_{ij,n+1}}{w_{ij,n} + w_{ij,n+1}}. \tag{C.11}$$

For the outer throat sections it is:

$$r_{ij,z,z+1} = r_{ij,n}, \tag{C.12}$$

$$w_{ij,z,z+1} = w_{ij,n}. \tag{C.13}$$

The dimensions of the pseudo pore throats are important to calculate the transmissibility, which influences the advective flux. Further the cross-sectional area of the pseudo pore throat can be calculated, which is used to calculate the diffusive fluxes:

$$\text{circular} : A_{ij,z,z+1} = \pi r^2_{ij,z,z+1}, \tag{C.14}$$

$$\text{rectangular} : A_{ij,z,z+1} = w_{ij,z,z+1}h_{ij,z,z+1}. \tag{C.15}$$

Acknowledgements This work was financially supported by the German Research Foundation (DFG), within the Collaborative Research Center on Interface-Driven Multi-Field Processes in Porous Media (SFB 1313, Project Number 327154368). This study was supported by the Special Research Fund (BOF) of Hasselt University, Project BOF22KV03.

Funding Open Access funding enabled and organized by Projekt DEAL. This work was financially supported by the German Research Foundation (DFG), within the Collaborative Research Center on Interface-Driven Multi-Field Processes in Porous Media (SFB 1313, Project Number 327154368).

Code availability The source code used to perform the simulations in this paper as well as the scripts to run the simulations and generate the plots are published in the following git-repository: https://git.iws.uni-stuttgart.de/dumux-pub/schollenberger2024a.

Declarations

Conflict of interest The author declare that they have no conflict of interest and no relevant financial or non-financial interests to disclose.

References

Agosti, A., Formaggia, L., Scotti, A.: Analysis of a model for precipitation and dissolution coupled with a Darcy flux. Journal of Mathematical Analysis and Applications **431**(2), 752–781 (2015). https://doi.org/10.1016/j.jmaa.2015.06.003

Bastian, P., Blatt, M., Dedner, A., et al.: The Dune framework: Basic concepts and recent developments. Computers & Mathematics with Applications **81**, 75–112 (2021). https://doi.org/10.1016/j.camwa.2020.06.007

Blunt, M.: Multiphase Flow in Permeable Media: A Pore-Scale Perspective. Cambridge University Press, Cambridge, (2017). https://doi.org/10.1017/9781316145098

Blunt, M.J., Jackson, M.D., Piri, M., et al.: Detailed physics, predictive capabilities and macroscopic consequences for pore-network models of multiphase flow. Advances in Water Resources **25**(8), 1069–1089 (2002). https://doi.org/10.1016/S0309-1708(02)00049-0

Bringedal, C., Kumar, K.: Effective behavior near clogging in upscaled equations for non-isothermal reactive porous media flow. Transport in Porous Media **120**(3), 553–577 (2017). https://doi.org/10.1007/s11242-017-0940-y

Bringedal, C., Berre, I., Pop, I.S., et al.: Upscaling of nonisothermal reactive porous media flow under dominant péclet number: The effect of changing porosity. Multiscale Modeling & Simulation **14**(1), 502–533 (2016). https://doi.org/10.1137/15M1022781

Bringedal, C., Von Wolff, L., Pop, I.S.: Phase field modeling of precipitation and dissolution processes in porous media: upscaling and numerical experiments. Multiscale Modeling & Simulation **18**(2), 1076–1112 (2020). https://doi.org/10.1137/19M1239003

Bruus, H.: Acoustofluidics 1: Governing equations in microfluidics. Lab on a Chip **11**, 3742–3751 (2011). https://doi.org/10.2136/vzj2010.0026

Cahn, J., Hilliard, J.: Free energy of a nonuniform system. i. interfacial free energy. Journal of Chemical Physics **28**(28), 258–267 (1958). https://api.semanticscholar.org/CorpusID:98613100

Daliakopoulos, I., Tsanis, I., Koutroulis, A., et al.: The threat of soil salinity: A european scale review. Science of The Total Environment **573**, 727–739 (2016). https://doi.org/10.1016/j.scitotenv.2016.08.177

Dashtian, H., Shokri, N., Sahimi, M.: Pore-network model of evaporation-induced salt precipitation in porous media: The effect of correlations and heterogeneity. Advances in Water Resources **112**, 59–71 (2018). https://doi.org/10.1016/j.advwatres.2017.12.004

Eden, M., Nikolopoulos, C., Muntean, A.: A multiscale quasilinear system for colloids deposition in porous media: weak solvability and numerical simulation of a near-clogging scenario. Nonlinear Analysis: Real World Applications **63**, 103,408, 29 (2022). https://doi.org/10.1016/j.nonrwa.2021.103408

Espinosa, R., Franke, L., Deckelmann, G.: Model for the mechanical stress due to the salt crystallization in porous materials. Construction and Building Materials **22**(7), 1350–1367 (2008). https://doi.org/10.1016/j.conbuildmat.2007.04.013

Gahn, M., Pop, I.S.: Homogenization of a mineral dissolution and precipitation model involving free boundaries at the micro scale. Journal of Differential Equations **343**, 90–151 (2023). https://doi.org/10.1016/j.jde.2022.10.006

Golparvar, A., Zhou, Y., Wu, K., et al.: A comprehensive review of pore scale modeling methodologies for multiphase flow in porous media. Advances in Geo-Energy Research **2**(4), 418–440 (2018). https://doi.org/10.26804/ager.2018.04.07

Jambhekar, V.A., Helmig, R., Schröder, N., et al.: Free-flow-porous-media coupling for evaporation-driven transport and precipitation of salt in soil. Transport in Porous Media **110**, 251–280 (2015). https://doi.org/10.1007/s11242-015-0516-7

Jambhekar, V.A., Mejri, E., Schröder, N., et al.: Kinetic approach to model reactive transport and mixed salt precipitation in a coupled free-flow-porous-media system. Transport in Porous Media **114**(2), 341–369 (2016). https://doi.org/10.1007/s11242-016-0665-3

Joekar-Niasar, V., Hassanizadeh, S.M., Leijnse, A.: Insights into the relationships among capillary pressure, saturation, interfacial area and relative permeability using pore-network modeling. Transport in Porous Media **74**(2), 201–219 (2010). https://doi.org/10.1007/s11242-007-9191-7

Kala, K., Voskov, D.: Element balance formulation in reactive compositional flow and transport with parameterization technique. Computational Geosciences **24**(2), 609–624 (2020). https://doi.org/10.1007/s10596-019-9828-y

Kang, Q., Zhang, D., Chen, S.: Simulation of dissolution and precipitation in porous media. Journal of Geophysical Research: Solid Earth **108**(B10), (2003). https://doi.org/10.1029/2003JB002504

Kelm, M., Gärttner, S., Bringedal, C., et al.: Comparison study of phase-field and level-set method for three-phase systems including two minerals. Computational Geosciences **26**(3), 545–570 (2022). https://doi.org/10.1007/s10596-022-10142-w

Koch, T., Gläser, D., Weishaupt, K. et al.: Dumux 3.0.0 (2018). https://doi.org/10.5281/zenodo.2479595

Koch, T., Gläser, D., Weishaupt, K., et al.: Dumux 3 - an open-source simulator for solving flow and transport problems in porous media with a focus on model coupling. Computers and Mathematics with Applications (2020). https://doi.org/10.1016/j.camwa.2020.02.012

Kumar, K., van Noorden, T.L., Pop, I.S.: Effective dispersion equations for reactive flows involving free boundaries at the microscale. Multiscale Modeling & Simulation **9**(1), 29–58 (2011). https://doi.org/10.1137/100804553

Li, L., Peters, C.A., Celia, M.A.: Upscaling geochemical reaction rates using pore-scale network modeling. Advances in Water Resources **29**(9), 1351–1370 (2006). https://doi.org/10.1016/j.advwatres.2005.10.011

Liu, H., Kang, Q., Leonardi, C.R., et al.: Multiphase lattice Boltzmann simulations for porous media applications. Computational Geosciences **20**(4), 777–805 (2016). https://doi.org/10.1007/s10596-015-9542-3

Luo, H., Quintard, M., Debenest, G., et al.: Properties of a diffuse interface model based on a porous medium theory for solid-liquid dissolution problems. Computational Geoscience **16**(4), 913–932 (2012). https://doi.org/10.1007/s10596-012-9295-1

Mejri, E., Bouhlila, R., Helmig, R.: Heterogeneity effects on evaporation-induced halite and gypsum co-precipitation in porous media. Transport in Porous Media **118**,(2017). https://doi.org/10.1007/s11242-017-0846-8

Mejri, E., Helmig, R., Bouhlila, R.: Modeling of evaporation-driven multiple salt precipitation in porous media with a real field application. Geosciences **10**(10), (2020). https://www.mdpi.com/2076-3263/10/10/395

Molins, S.: Reactive Interfaces in Direct Numerical Simulation of Pore-Scale Processes. Reviews in Mineralogy and Geochemistry **80**(1), 461–481 (2015). https://doi.org/10.2138/rmg.2015.80.14

Molins, S., Trebotich, D., Steefel, C.I., et al.: An investigation of the effect of pore scale flow on average geochemical reaction rates using direct numerical simulation. Water Resources Research **48**(3), (2012) https://doi.org/10.1029/2011WR011404

Munns, R., Tester, M.: Mechanisms of salinity tolerance. Annual review of plant biology **59**, 651–681 (2008). https://doi.org/10.1146/annurev.arplant.59.032607.092911

Nogues, J.P., Fitts, J.P., Celia, M.A., et al.: Permeability evolution due to dissolution and precipitation of carbonates using reactive transport modeling in pore networks. Water Resources Research **49**(9), 6006–6021 (2013). https://doi.org/10.1002/wrcr.20486

Norouzi Rad, M., Shokri, N., Sahimi, M.: Pore-scale dynamics of salt precipitation in drying porous media. Physical Review E **88**(032), 404 (2013). https://doi.org/10.1103/PhysRevE.88.032404

Ondrasek, G., Rengel, Z., Veres, S.: Soil salinisation and salt stress in crop production. In: Shanker, A.K., Venkateswarlu, B. (eds.) Abiotic Stress in Plants - Mechanisms and Adaptations, pp. 171–190. InTech, Rijeka, Croatia (2011). https://doi.org/10.5772/22248

Pérez-Villaseñor, F., Iglesias-Silva, G.A., Hall, K.R.: Osmotic and activity coefficients using a modified pitzer equation for strong electrolytes 1:1 and 1:2 at 298.15 k. Industrial & Engineering Chemistry Research **41**(5), 1031–1037 (2002). https://doi.org/10.1021/ie0103153

Qadir, M., Quillérou, E., Nangia, V., et al.: Economics of salt-induced land degradation and restoration. Natural Resources Forum **38**(4), 282–295 (2014). https://doi.org/10.1111/1477-8947.12054

Rad, M.N., Shokri, N., Keshmiri, A., et al.: Effects of grain and pore size on salt precipitation during evaporation from porous media. Transport in Porous Media **110**(2), 281–294 (2015). https://doi.org/10.1007/s11242-015-0515-8

Raoof, A., Hassanizadeh, S.M.: A new method for generating pore-network models of porous media. Transport in Porous Media **81**(3), 391–407 (2010). https://doi.org/10.1007/s11242-009-9412-3

Raoof, A., Hassanizadeh, S.M., Leijnse, A.: Upscaling transport of adsorbing solutes in porous media: Pore-network modeling. Vadose Zone Journal **9**(3), 624–636 (2010). https://doi.org/10.2136/vzj2010.0026

Rengasamy, P.: World salinization with emphasis on Australia. Journal of Experimental Botany **57**(5), 1017–1023 (2006). https://doi.org/10.1093/jxb/erj108

Rohde, C., Von Wolff, L.: A ternary Cahn-Hilliard-Navier-Stokes model for two-phase flow with precipitation and dissolution. Mathematical Models and Methods in Applied Sciences **31**(01), 1–35 (2021). https://doi.org/10.1142/S0218202521500019

Scherer, G.W.: Stress from crystallization of salt. Cement and Concrete Research **34**(9), 1613–1624 (2004). https://doi.org/10.1016/j.cemconres.2003.12.034. (**h. F. W. Taylor Commemorative Issue**)

Schulz, R., Ray, N., Frank, F., et al.: Strong solvability up to clogging of an effective diffusion-precipitation model in an evolving porous medium. European Journal of Applied Mathematics **28**(2), 179–207 (2017). https://doi.org/10.1017/S0956792516000164

Shahid, S.A., Zaman, M., Heng, L.: Soil salinity: Historical perspectives and a world overview of the problem. In: Guideline for Salinity Assessment, Mitigation and Adaptation Using Nuclear and Related Techniques. Springer International Publishing, Cham, pp. 43–53 (2018). https://doi.org/10.1007/978-3-319-96190-3_2

Sharma, D.K., Singh, A.: Salinity research in India-achievements, challenges and future prospects. Water and Energy International **58**(6), 35–45 (2015). http://krishi.icar.gov.in/jspui/handle/123456789/3367

Shokri, N.: Pore-scale dynamics of salt transport and distribution in drying porous media. Physics of Fluids **26**(1), 012,106 (2014). https://doi.org/10.1063/1.4861755

Singh, A.: Soil salinization and waterlogging: A threat to environment and agricultural sustainability. Ecological Indicators **57**, 128–130 (2015). https://doi.org/10.1016/j.ecolind.2015.04.027

Steefel, C.I., Molins, S., Trebotich, D.: Pore Scale Processes Associated with Subsurface CO2 Injection and Sequestration. Reviews in Mineralogy and Geochemistry **77**(1), 259–303 (2013). https://doi.org/10.2138/rmg.2013.77.8

Weishaupt, K.: Model concepts for coupling free flow with porous medium flow at the pore-network scale: From single-phase flow to compositional non-isothermal two- phase flow. Universität Stuttgart - Stuttgart: Institut für Wasser- und Umweltsystemmodellierung doi:http://dx.doi.org/10.18419/opus-10932 (2020)

Weishaupt, K., Joekar-Niasar, V., Helmig, R.: An efficient coupling of free flow and porous media flow using the pore-network modeling approach. Journal of Computational Physics: X **1**(100), 011 (2019). https://doi.org/10.1016/j.jcpx.2019.100011

Weishaupt, K., Koch, T., Helmig, R.: A fully implicit coupled pore-network/free-flow model for the pore-scale simulation of drying processes. Drying Technology **40**(4), 697–718 (2022). https://doi.org/10.1080/07373937.2021.1955706

Wicke, B., Smeets, E., Dornburg, V., et al.: The global technical and economic potential of bioenergy from salt-affected soils. Energy & Environmental Science **4**, 2669–2681 (2011). https://doi.org/10.1039/C1EE01029H

van Noorden, T.L.: Crystal precipitation and dissolution in a porous medium: effective equations and numerical experiments. Multiscale Modeling & Simulation **7**(3), 1220–1236 (2008). https://doi.org/10.1137/080722096

van Noorden, T.L.: Crystal precipitation and dissolution in a thin strip. European Journal of Applied Mathematics **20**(1), 69–91 (2009). https://doi.org/10.1017/S0956792508007651

van Noorden, T.L., Eck, C.: Phase field approximation of a kinetic moving-boundary problem modelling dissolution and precipitation. Interfaces and Free Boundaries **13**(1), 29–55 (2011). https://doi.org/10.4171/IFB/247

von Wolff, L., Pop, I.S.: Upscaling of a Cahn-Hilliard Navier-Stokes model with precipitation and dissolution in a thin strip. J Fluid Mech **941**, A49, 37 (2022). https://doi.org/10.1017/jfm.2022.308

von Wolff, L., Weinhardt, F., Class, H., et al.: Investigation of crystal growth in enzymatically induced calcite precipitation by micro-fluidic experimental methods and comparison with mathematical modeling. Transport in Porous Media **137**(2), 327–343 (2021). https://doi.org/10.1007/s11242-021-01560-y

Yang, J., Lei, T., Wang, G., et al.: Lattice boltzmann modelling of salt precipitation during brine evaporation. Advances in Water Resources **180**(104), 542 (2023). https://doi.org/10.1016/j.advwatres.2023.104542

Yoon, H., Kang, Q., Valocchi, A.J.: Lattice Boltzmann-Based Approaches for Pore-Scale Reactive Transport. Reviews in Mineralogy and Geochemistry **80**(1), 393–431 (2015). https://doi.org/10.2138/rmg.2015.80.12

Zaretskiy, Y., Geiger, S., Sorbie, K., et al.: Efficient flow and transport simulations in reconstructed 3d pore geometries. Advances in Water Resources **33**(12), 1508–1516 (2010). https://doi.org/10.1016/j.advwatres.2010.08.008